Supplementary Information for

Layer and rhythm specificity for Predictive Routing

André M. Bastos, Mikael Lundqvist, Ayan S. Waite, Nancy Kopell, Earl K. Miller

Corresponding author: André M. Bastos

Correspondence: andrembastos@gmail.com, nk@math.bu.edu, ekmiller@mit.edu

This PDF file includes:

Experimental Procedures

Lead Contact and Materials Availability

The Lead Contact for this study is Earl Miller (ekmiller@mit.edu). Requests for materials should be directed to the Lead Contact. This study did not generate novel reagents.

Experimental Model and Subject Details

Two adult rhesus macaques (*macaca mulatta*) were used in this study (Monkey S: 6 years old, 5.0 kg and monkey L: 17 years old, 10.5 kg). Both animals were pair-housed on 12-hr day/night cycles and maintained in a temperature-controlled environment (80°F). All procedures were approved by the MIT IACUC and followed the guidelines of the MIT Animal Care and Use Committee and the US National Institutes of Health.

Methods Details

Surgical Procedures

All procedures were performed in a sterile surgical suite, with animals under full general anesthesia. Animals were first anesthetized with ketamine and then intubated. They were maintained in a stable plane of anesthesia with sevofluorane. After each procedure, animals received analgesic and antibiotic medications. Three surgical procedures were performed per monkey. First, a titanium head post was fixed to the posterior part of the cranium with titanium screws. The head post was allowed to integrate into the bone for at least 8 months prior to the next surgery. Second, a custom-machined Carbon PEEK chamber system with three recording wells (placed over prefrontal, parietal, and visual cortex) was affixed to the cranium, also with titanium screws. After a one-month period, a third procedure was

www.pnas.org/cgi/doi/10.1073/pnas.2014868117

performed, in which three craniotomies ranging in circular diameter between 10-16 mm^2 were opened inside each recording well.

Lowering procedure and laminar placement of electrodes

Traditionally, studies with laminar probes have used Current Source Density (CSD) mapping to identify the position of layer 4. However, for parietal area 7A, to our knowledge there is no published study using this technique. Therefore, we chose to align our data to the pial surface of the cortex, a technique that has been previously used to separate recording channels into superficial vs. deep layers in monkeys for recordings in parietal and prefrontal cortex (1). This was the most robust laminar alignment metric that could be applied to visual, parietal, and prefrontal cortex with minimal assumptions. The average cortical thickness for the recorded regions was 2.4mm, measured using MRI, and visually measuring the gray matter thickness using Osirix software (Geneva, Switzerland). Superficial layer channels were classified from the top of cortex to a depth of 1.2 mm, and deep layer channels from 1.2 to 2.4mm. This maps approximately onto layers 1-4 for superficial, and 5-6 for deep.

We first punctured the dura using a guide tube. Then we lowered the laminar probes through the guide tube using custom-built drives that advanced with a turn screw system. In order to place the contacts of the laminar probe uniformly through the cortex, spanning from cerebrospinal fluid through the gray matter to the white matter, we used a number of physiologic indicators to guide our electrode placement, as previously described (2). First, the presence of a slow 1-2 Hz signal, a heartbeat artifact, was often found as we pierced the pia mater and just as we entered the gray matter. Second, as the first contacts of the electrode entered the gray matter, the magnitude of the local field potential increased, and single units and/or neural hash became apparent, both audibly and visually with spikes appearing in the online spike threshold crossing. Once the tip of the electrode transitioned into the gray matter, electrodes were lowered slowly an additional ~2.5mm. At this point, we retracted the probe by 200-400 um, and allowed the probe to settle for between one to two hours before beginning the task. We left between 1-3 contacts out of gray matter in the overlying Cerebral Spinal Fluid (CSF).

Multi-Unit Activity Extraction and Spike-Sorting

For the analysis of the analog multi-unit activity (MUA) we band-pass filtered the raw, unfiltered, 30kHz sampled data into a wide band between 500-5,000Hz, the power range dominated by spikes. The signal was then low-pass filtered at 250Hz and re-sampled to 1,000 kHz. The advantage of this signal is that it captures all nearby units, including those with low signal to noise ratio that would not be captured with a strict threshold.

For the analysis of thresholded spikes, we first placed an online threshold manually on each recording session to ensure each recording channel captured waveforms with sufficient signal to noise ratio to qualify as neuronal spiking. These were typically placed at between 2-4 standard deviations away from the noise floor. Offline, spike sorting was performed manually using Plexon offline sorter. We projected the waveform shapes into the top 2 or 3 principle components, and sorted each electrode's threshold crossings into isolatable waveforms. We included these single units into analysis if their average firing rate per trial (between 1.5 seconds pre-sample to 1.5 seconds post-sample) was stable for at least 120 trials. We defined stability with the Matlab function findchangepts().

Local Field Potential power, coherence and Granger causality analysis

All analyses were performed with customized MATLAB scripts and with Fieldtrip software (3). Bipolar derivation is a recommended pre-step prior to Granger causality and coherence analysis, as the presence of a common reference can lead to spurious results (4, 5). In addition, bipolar derivation enhances the spatial localization of LFP signals and removes the common reference and any common noise or volume conduction in the signal (6). Here, we computed the sample-by-sample bipolar differences by subtracting contacts that at a distance of 400um: next-nearest neighbors for the laminar probe data spaced at 200um between contacts, and next-next-nearest neighbors for the probe data spaced at 100um between contacts.

We then estimated power, coherence, and Granger causality on these bipolar derivations. We estimated power at all frequencies from 0-250 Hz using multitaper spectral estimation (smoothing window of 5Hz, leading to 9 tapers per spectral estimate, using window sizes of 1 second (0 to 1 seconds relative to sample onset is the period of visual stimulation, -1 to 0 seconds relative to sample onset is the pre-stimulus fixation interval) per trial. These Fourier coefficients were then used to calculate the Cross-Spectral Density matrix, from which we derived coherence and non-parametric spectral Granger causality (see below).

The computation of Granger causality in the frequency domain requires the estimation of two quantities: the spectral transfer matrix ($H(\omega)$), which is frequency dependent, and the covariance of the model's residuals (Σ). The spectral transfer matrix defines how power in one channel is transferred to other channels, at each temporal lag. The model's residuals is not a function of frequency, and defines the amount of variance that is left unexplained by the linear model, $H(\omega)$. Traditionally, $H(\omega)$ is computed in a parametric (model-based) fashion by first fitting an autoregressive model to the data, and then Fourier transforming the model (7). However, it is also possible to compute, $H(\omega)$, and thus Granger causality, directly from the spectral transform of the data. In brief, the following fundamental identity holds: $H(\omega)\Sigma H(\omega)^* = S(\omega)$, with $S(\omega)$ being the cross-spectral density matrix at frequency ω. Starting from the cross-spectral density matrix ($S(\omega)$) it is possible to factorize the cross-spectral density matrix into a noise covariance matrix (Σ) and spectral transfer matrix ($H(\omega)$) by applying spectral matrix factorization (8) —which provides the necessary ingredients for calculating Granger causality. The nonparametric estimation of GC has certain advantages over parametric approaches in that it does not require the specification of a particular autoregressive model order.

Statistical Testing

We computed whether the MUA, power, coherence, and Granger causality was systematically different between conditions (Predictable vs. Unpredictable). To do this, we calculated either the mean difference or percent change for each channel or inter-areal channel-pair of Predictable vs. Unpredictable sampling. We then quantified whether this raw difference or percent change was significant by performing a nonparametric randomization test (9). Per channel (for MUA and LFP power) or channel-pair (for coherence and Granger) we randomized the experimental label (Predictable vs. Unpredictable sampling). We performed this randomization 1,000 times. For each randomization, we took the number of consecutive time bins (in the case of MUA) or frequency bins (for power, coherence, and GC) that passed a first level criteria. This first level criteria was that two measures (for example, LFP power when comparing unpredictable vs. predictable cuing) had to differ from one another at significance value of $P<0.01$, uncorrected, based on a t-test statistic. The maximum positive or negative cluster was determined for each randomization. This step controls for multiple comparisons across neighboring (and

possible correlated) time or frequency bins. Finally, these clusters from the randomization distribution were used to determine significance values for the empirically observed clusters, using a P-value of 0.05, corrected for multiple comparisons.

For determining differences between superficial vs. deep layers, we first averaged the corresponding metric (power, coherence, Granger causality) across the particular frequency band (theta, alpha, beta, gamma) for all superficial and deep channels/channelpairs. Then we performed a Wilcoxon rank sum test to determine significant differences across the populations with an alpha at $p<0.05$.

For determining the difference between feedforward vs. feedback Granger causality modulation, we determined the percentage of modulated inter-areal directed functional connections, integrating all frequencies in the theta, alpha/beta, and gamma frequency bands. We then applied a Chi-squared test for differences in percentage to test whether e.g., feedforward functional connections were more modulated (had a greater percentage) than feedback functional connections.

Data and Code Availability

The data and code will be made available by reasonable request by contacting the lead author, Earl Miller (ekmiller@mit.edu).

Supplemental References

1. K. Johnston, L. Ma, L. Schaeffer, S. Everling, Alpha Oscillations Modulate Preparatory Activity in Marmoset Area 8Ad. *J. Neurosci.* **39**, 1855–1866 (2019).

2. A. M. Bastos, R. Loonis, S. Kornblith, M. Lundqvist, E. K. Miller, Laminar recordings in frontal cortex suggest distinct layers for maintenance and control of working memory. *PNAS*, 201710323 (2018).

3. R. Oostenveld, P. Fries, E. Maris, J.-M. Schoffelen, FieldTrip: Open source software for advanced analysis of MEG, EEG, and invasive electrophysiological data. *Comput Intell Neurosci* **2011**, 156869 (2011).

4. A. Trongnetrpunya, *et al.*, Assessing Granger Causality in Electrophysiological Data: Removing the Adverse Effects of Common Signals via Bipolar Derivations. *Front Syst Neurosci* **9**, 189 (2015).

5. M. Vinck, *et al.*, How to detect the Granger-causal flow direction in the presence of additive noise? *Neuroimage* **108**, 301–318 (2015).

6. A. M. Bastos, J.-M. Schoffelen, A Tutorial Review of Functional Connectivity Analysis Methods and Their Interpretational Pitfalls. *Front Syst Neurosci* **9**, 175 (2015).

7. M. Ding, Y. Chen, S. L. Bressler, "Granger causality: basic theory and application to neuroscience" in *Handbook of Time Series Analysis: Recent Theoretical Developments and Applications*, B. Schelter, M. Winterhalder, T. Timmer, Eds. (Wiley-VCH Verlag GmbH & Co. KGaA, 2006), pp. 437–460.

8. M. Dhamala, G. Rangarajan, M. Ding, Estimating Granger Causality from Fourier and Wavelet Transforms of Time Series Data. *Physical Review Letters* **100**, 018701 (2008).

9. E. Maris, R. Oostenveld, Nonparametric statistical testing of EEG- and MEG-data. *J. Neurosci. Methods* **164**, 177–190 (2007).

Supplemental Results

Relationship between spiking and LFP power

To test whether neurons with enhanced spiking to unpredictable samples tended to be at recording sites that also showed modulation of LFP power, we computed the correlation between modulation of spiking and LFP power by unpredictable vs unpredictable samples from -1.25 to +1.25 seconds relative to sample onset. We took care to avoid selecting the same recording sites for spiking as for LFP power (to avoid spike-to-LFP bleedthrough, which would create spurious correlations). Instead, we compared a particular site's spiking to the LFP of the bipolar difference between LFPs at two adjacent recording sites (bipolar spacing was 400 um, see Methods). The correlation was performed for each electrode separately, and then averaged across areas/layers.

In all areas, modulations of spiking and LFP gamma were positively correlated across sites (Supplemental Figure 2A). In the three areas with laminar-resolved recordings, the correlation between spiking and gamma modulation was stronger in superficial than deep layers (Wilcoxon rank sum test comparing unit-by-unit correlation between power and MUA in superficial vs. deep layers, $P<0.05$, Supplemental Figure 2B). In the beta-band, the correlation was negative in all areas except superficial layers of area 7A (Supplemental Figure 2C) . In the alpha band, the correlation between power and MUA was negative in all areas, and in V4, it was stronger in deep cortical layers (Wilcoxon rank sum test comparing unit-by-unit correlation between power and MUA in superficial vs. deep layers, $P<0.05$, Supplemental Figure 2D). In the theta-band, effects by areas and layer were mixed. The correlation between spiking and LFP modulation was positive in V4 and not layer specific. It was around zero in 7A, and slightly negative in PFC superficial layers (Supplemental Figure 2E), where the correlation was different between superficial and deeper layers (Supplemental Figure 2E, Wilcoxon rank sum test comparing unit-by-unit correlation between power and MUA in superficial vs. deep layers, $P<0.05$).

Stimulus specificity of LFP power modulation in the pre-sample interval

We also examined stimulus selectivity during the pre-sample interval for Predictable blocks (because the sample object was only predictable on Predictable blocks). To compute selectivity, we contrasted the percent change in pre-sample power for each site's most preferred vs. least preferred sample when it was being predicted. Positive values indicate more power for the site's preferred stimulus when it was predicted (compared to when it was not predicted). Negative values indicate less power for the site's preferred stimulus when it was predicted (compared to when it was not predicted). In the gamma-band for only superficial layers, there was less pre-sample power when the preferred sample was predicted compared to when it was not ($P<0.001$, sign test, Supplemental Figure 4F). In addition, directly comparing gamma selectivity in superficial vs. deep layers revealed a significant difference (Wilcoxon rank sum test, $P<0.05$). In the alpha and beta bands, there was greater pre-sample power when the preferred sample was predicted compared to when it was not, but only in deep layers ($P<1E-6$ for alpha in deep layers, $P<1E-3$ for beta in deep layers, $P>0.05$ for alpha in superficial layers, $P>0.05$ for beta in superficial layers, sign test, Supplemental Figure 4G/H). Power in the theta band in the pre-sample interval was not different for the preferred vs. non-preferred sample ($P>0.05$ for both superficial and deep, sign test, Supplemental Figure 4H).

Modulation of theta/beta/gamma power after controlling for sample repetition

Power modulation during the sample interval could, in principle, simply be consequence of the same sample object being repeated across trials (during Predictable blocks) vs. not (during Unpredictable blocks). If neuronal modulation by predictability was due entirely to passive synaptic adaptation to repeated inputs, neural effects should be accounted for by how much time has passed between repetitions of the same sample. This time was different between blocks. During Predictable blocks, the median time between sample presentation on one trial and repetition of the same sample object (on the next trial) was seven seconds. During Unpredictable blocks, the median time between repetition of the same sample object was 20 seconds. To control for this difference, we stratified the distributions of inter-sample intervals (ISI) to equalize the medians. Iteratively, we removed the largest ISI trial from the distribution of trials during the Unpredictable blocks and the shortest ISI trial from the Predictable blocks, until the medians of the two block types were matched. We then computed the percent change in power between Unpredictable vs. Predictable blocks on this stratified dataset (black lines in Supplemental Figure 5) and compared it to the original dataset (red lines in Supplemental Figure 5).

There was an effect of time between repetitions per se but the effects of Predictable vs Unpredictable blocks largely remained after accounting for it. The differences in power in all areas for the beta and gamma bands between Predictable vs Unpredictable blocks remained significant even after equating the ISIs ($P<0.05$, Supplemental Figure 5, cluster-based randomization test, red horizontal lines indicate significant power modulation of original dataset, black horizontal lines indicate significant power modulation of ISI control dataset). The exception to this was alpha/beta modulation in V4, where neural modulation due to predictability could be accounted for by time between sample repetition (Supplemental Figure 5A). Beta/gamma modulation in PFC and gamma modulation in FEF were unaffected by sample ISI (Supplemental Figure 5 F,G). Beta modulation in FEF was slightly *greater* after controlling for sample ISI (Supplemental Figure 5G). Theta was only significant in area V4 after accounting for ISI ($P<0.05$, Supplemental Figure 5A-E, cluster-based randomization test).

Violation of predictions

During Predictable blocks, a strong expectation of a specific sample object could build. Then, when there was a switch to an Unpredictable block, that expectation was violated for at least the first few trials. We examined the LFP power as a function of the number of trials since a switch from a Predictable to an Unpredictable block. This revealed strong gamma increases in all areas that were maximal within the first few trials of such a "violation" of expectation (Supplemental Results, Supplemental Figure 6A). In area V4, the gamma band response remained elevated above the predictable response for the entire Unpredictable block. By contrast, PFC gamma to unpredictable samples remained elevated above that to predictable samples for the first 15-20 trials. The other areas fell in between. Alpha and beta modulation was also strongest during the violation and subsequent trials (Supplemental Figure 6B). In PFC alpha/beta power remained suppressed almost throughout the entire Unpredictable block (relative to Predictable blocks), while it was more transiently modulated in the other areas. These analyses suggest that cortex is in its most excitable state immediately following transition from predictable to unpredictable sample objects, reflecting a violation of expectation.

Modulation of LFP power tracks behavior during Predictable blocks

During Predictable blocks, there was an increase in alpha/beta power compared to Unpredictable blocks. We also observed better behavioral performance on Predictable blocks. We therefore next asked whether behavioral improvement within the Predictable block correlated with increased alpha/beta power (or any other frequencies). First, by analyzing performance relative to trial number within the Predictable blocks, we confirmed that behavioral improvement peaked around 15-20 trials after the beginning of the Predictable block. It remained relatively stable for the remainder of the block (Supplemental Figure 8A). We correlated power during the sample interval from 1-100 Hz to behavioral accuracy computed over a sliding window of five trials. This revealed that beta power in V4, FEF, and PFC was positively correlated to accuracy within Predictable blocks ($P<0.05$, Supplemental Figure 8B, cluster-based randomization test). This analysis also showed that all areas showed significant negative correlations between behavior and power in the theta and gamma ranges ($P<0.05$, Supplemental Figure 8B, cluster-based randomization test).

Predictability modulates inter-area coherence

We calculated coherence from 1-100 Hz between bipolar-derivations of LFPs across all combinations of areas (see Methods). Modulation of coherence by predictability (Unpredictable minus Predictable, in z-score units, N=20,384 inter-areal bipolar site pairs) between one example pair of areas, V4 and FEF, is shown in Supplemental Figure 9A (all area pairs are shown in Supplemental Figure 10). In gamma/theta, there was greater coherence (positive values) during presentation of unpredictable samples (red bars indicate significance, $P<0.05$, corrected for multiple comparisons, cluster-based randomization). By contrast, in alpha/beta, there was greater coherence during predictable samples (negative numbers, blue bars, Supplemental Figure 9A, $p<0.05$, cluster-based randomization).

Similar effects were seen across the entire network of areas. Supplemental Figure 9B shows the percentage of modulated connections across the network, where the total number of possible connections is 15, counting within-area connections (see Supplemental Figure 10 for each individual connection). Both gamma (40-90 Hz) and theta (2-6Hz) coherence were higher during unpredictable than predictable samples (Supplemental Figure 9B, red line). Alpha and beta coherence showed the opposite (Supplemental Figure 9B, blue line). Supplemental Figure 9C shows effects of coherence for each area to the rest, with colors representing the number of significantly modulated connections ($P<0.05$, cluster-based randomization). The network of significantly modulated coherence links is shown in Supplemental Figure 9D-G. Red indicates greater coherence during unpredictable samples. Blue indicates greater coherence during predictable samples. Line thickness indicates the strength of effect in z-score units (see Methods). The boxes indicate within-area coherence. Every area showed some modulation of coherence by sample predictability (Supplemental Figure 9). There was more gamma (and theta, with one exception) coherence during unpredictable samples and more alpha/beta coherence during predictable samples. But note that, as in the power analysis (see above), area 7A was an outlier in the beta band, showing greater within- and across-area coherence to unpredictable samples (Supplemental Figure 9F). V4-PFC was also an outlier in the alpha/beta band, showing enhanced coherence during unpredictable samples.

There were also differences in coherence between layers. In the gamma band, the superficial layers of V4 and PFC showed a greater increase in coherence during Unpredictable samples (positive numbers, Supplemental Figure 9H, $P<0.05$, Wilcoxon rank sum test, comparing all coherence modulations in superficial vs. deep layers) as did superficial-layer V4 and 7A theta coherence (Supplemental Figure 9K,

P<0.05, Wilcoxon rank sum test, comparing all coherence modulations in superficial vs. deep layers). There were increases in superficial-layer beta coherence between each area and the network. In 7A, it was during unpredictable samples. For PFC, it was during predictable samples (Supplemental Figure 9I, P<1E-16 for 7A and P<1E-21 for PFC, Wilcoxon rank sum test, comparing all coherence modulations in superficial vs. deep layers).

Effects were also seen during the pre-sample interval but they were different from that during the sample. Supplemental Figure 11A shows the percentage of coherence links modulated by sample predictability with greater coherence during unpredictable blocks shown in red and predictable blocks shown in blue. The modulation of gamma-band coherence was very low. This was expected because there was no bottom-up sensory input. But the pattern of effects for beta and theta coherence were the opposite of that seen during the sample. Theta coherence was greater during Predictable than Unpredictable blocks (Supplemental Figure 11A for the pre-sample interval vs. Supplemental Figure 9B for the sample interval) while beta coherence was greater during Unpredictable blocks (Supplemental Figure 11A for the pre-sample interval vs Supplemental Figure 9A for the sample interval). Alpha coherence was greater during Predictable blocks during the pre-sample interval.

There were also layer-specific differences during the pre-sample interval. Deep-layer PFC showed significantly more beta coherence to the rest of the network than superficial layers for Predictable than Unpredictable blocks (Supplemental Figure 11C, second from the top subpanel, P<0.05, Wilcoxon rank sum test comparing all coherence modulations in superficial vs. deep layers). By contrast, superficial-layer V4 showed a greater increase in network theta/alpha coherence during Predictable than Unpredictable blocks (Supplemental Figure 11C lower subpanels for alpha and theta, P<0.05, Wilcoxon rank sum test comparing all coherence modulations in superficial vs. deep layers). No pre-sample gamma coherence differences exceeded +/- 2 Z-score units of difference between Predictable vs. Unpredictable blocks.

Supplemental Figure Legends

Supplemental Figure 1 | Unpredicted vs. predicted Multi-Unit Activity

For each area, the average MUA response to an unpredicted cue (red) vs. a predicted cue (blue). Mean +/- SEM across MUAs.

Supplemental Figure 2 | Correlation between MUA and LFP power by area and layer
A, Unpredicted minus predicted MUA difference correlation across time (-1.25 to 1.25 seconds from cue onset) to LFP power at each frequency from 0-100 Hz. Mean Spearman correlation across each area, +/- SEM. B-E, Average Spearman correlation between power and MUA in superficial (right orange subplots) vs. deep (left blue subplots) layers for B, gamma (40-90 Hz), C, beta (15-30 Hz), D, alpha (8-14 Hz), and E, theta (2-6 Hz). Mean +/- SEM. Red asterisk denotes significant (P<0.05) differences between superficial and deep layers.

Supplemental Figure 3 | Neural information in single units and power modulation by area

A. Sample information, quantified with Percent Explained Variance (PEV) by area during the sample processing interval (0.05 s-1s post cue onset). Mean +/- SEM across units. Red asterisk and horizontal

black bars indicate significant differences in total information between each area and V4. B. Same as A, but for the pre-sample interval (1.5 s – 0.05 s pre-sample interval). PEV was calculated between firing rates and the to-be-presented sample, during Predictable blocks. C. Difference in neural information (PEV) about the sample in Unpredictable minus Predictable blocks, in the pre-sample (left sub-panel) and sample (right sub-panel) intervals. Mean +/- SEM across single units in deep and superficial layers. Asterisk denotes significant differences between superficial and deep layers. Superficial (N=439) and Deep (N=340) neurons across all areas were combined for this analysis. D-G, Percent change in LFP power modulation (power in Unpredictable vs. Predictable blocks) by area during the sample interval, separately by theta, alpha, beta, and gamma bands. Red asterisks in D, F, and G indicate significant differences in power modulation between each area and V4. Red asterisks in E indicate significant differences in power modulation between PFC and the other areas.

Supplemental Figure 4 | Unpredicted vs. predicted Power by area during the pre-sample interval and area V4 selectivity in pre-sample interval

A-E, Percent change in power during the pre-sample interval, comparing Unpredicted vs. Predicted power. Red bars denote Unpredicted > Predicted power, blue bars Unpredicted < Predicted power, $P<0.05$, cluster-based randomization test corrected for multiple comparisons. F-I, Most vs. least preferred percent change in LFP power for the superficial and deep layers. F, gamma-band (40-90 Hz), G, beta band (15-30 Hz), H, alpha band (8-12 Hz), I, theta-band (2-6 Hz). Mean +/- 2 SEM. Red asterisk denotes a significantly non-zero median ($P<0.05$, sign test).

Supplemental Figure 5 | Unpredicted vs. Predicted power modulation after controlling for inter-sample interval

A-E, Modulation of Local Field Potential (LFP) power (percent change in power, Unpredictable vs. Predictable blocks) from 0-100 Hz during the 1 second sample processing interval. Red lines: Full dataset (ISI between same sample repetitions during Predictable blocks = 7 seconds, ISI between same sample repetitions during Unpredictable blocks = 20 seconds). Black lines: ISI control dataset after equalizing ISIs between Predictable and Unpredictable blocks (ISI between same sample repetitions during Predictable blocks = 10 seconds, ISI between same sample repetitions during Unpredictable blocks = 10 seconds). Mean across all available LFPs per area, +/- 1SEM across LFPs. Horizontal bars denote significance at $P< 0.05$ for Unpredictable vs. Predictable blocks in the Full dataset (red) and ISI control dataset (black), corrected for multiple comparisons. F-I, Percent change in LFP power for unpredictable vs. predictable samples in Full and ISI control datasets. F, gamma-band (40-90 Hz), G, beta-band (15-30 Hz), H, alpha-band (8-14 Hz), I, theta-band (2-6 Hz). Mean +/- SEM across LFPs.

Supplemental Figure 6 | Power change during Unpredictable blocks, locked to first violation trial

A. Unpredictable vs. Predictable power (percent change) in the gamma (40-90 Hz range, red lines) as a function of trial number within the Unpredictable block relative to the average of all Predictable block trials. Positive numbers indicate more power in the Unpredictable block. We define the first violation trial as the first trial in an Unpredictable block after a Predictable block. Mean +/- 2SEM across sessions (N=71). B. Same as A, but for the alpha (8-14 Hz, in blue) and beta (15-30 Hz, in green) bands.

Supplemental Figure 7 | Power change during Predictable blocks, locked to the first trial in a Predictable block

A. Predictable vs. Unpredictable power (percent change) in the gamma (40-90 Hz range, red lines) as a function of trial number within the Predictable blocks relative to the average of all Unpredictable trials. Positive numbers indicate more power in the Predictable block. Mean +/- 2SEM across sessions (N=71). B. Same as A, but for the alpha (8-14 Hz, green lines) and beta (15-30 Hz, blue lines) bands. Dotted vertical lines indicate the trial number with minimum (for gamma) or maximum power (for alpha and beta).

Supplemental Figure 8 | Correlation between behavior and power during predicted blocks

A, Mean accuracy (change from mean accuracy across the session) as a function of trial count since the start of all Predictable blocks. Error bars are 2 SEM across 71 sessions. B, Spearman correlation between the accuracy time course from A with power modulation only in Predictable blocks. Significant correlation values ($P<0.05$ corrected for multiple comparisons with cluster-based randomization testing) are marked with greater opacity and highlighted with black lines.

Supplemental Figure 9| Coherence networks during unpredicted vs. predicted sample processing

A. V4-FEF coherence z-score difference (unpredictable minus predictable) across all inter-area site pairs, N=20,384. Horizontal bars indicate significant ($P<0.05$, corrected for multiple comparisons) differences for unpredictable > predictable (red bars) and unpredictable < predictable (blue bars). B. Across all possible pairs of cortical areas (N=15, counting within-area connections), the percentage of significantly modulated connections (red: unpredictable > predictable, blue: unpredictable < predictable). C. The number of modulated connections per area as a function of frequency. D-G, Within and inter-area coherence modulations by band, for the theta (2-6 Hz, subpanel D), alpha (8-14 Hz, subpanel E), beta (15-30 Hz, subpanel F), and gamma (40-90 Hz, subpanel G) bands. The strength of modulation is represented by line thickness (see Legend). Edges represent inter-areal coherence modulation. Box outlines represent within-area coherence modulation (if colored). Unpredictable > Predictable coherence differences are in red lines/boxes, Predictable > Unpredictable coherence differences are in blue lines/boxes. H-K, Coherence z-score difference (unpredictable minus predictable) between each area and the rest, separately for superficial coherence to rest (orange bars) and deep coherence (blue bars) to rest (blue bars) for different frequency ranges (gamma: subpanel H, beta: subpanel I, alpha: subpanel J, theta: subpanel K). Mean +/- SEM, asterisks denote significant differences between layers.

Supplemental Figure 10 | Unpredicted vs. predicted Coherence spectra during the sample interval

Z-score of coherence difference: Unpredicted minus Predicted, divided by the standard error of the mean for each area combination. Red bars denote Unpredicted > Predicted coherence, blue bars Unpredicted < Predicted coherence, $p<0.05$, cluster-based randomization test. Mean +/- SEM across all bipolar LFP pairs for each inter-areal combination.

Supplemental Figure 11 | Coherence networks in the pre-sample interval

A. Across all possible pairs of cortical areas (N=25, counting within-area connections), the percentage of significantly modulated coherence connections (red: Unpredictable > Predictable, blue: Unpredictable < Predictable) in the pre-sample interval. B. The number of modulated coherence connections per area as a function of frequency in the pre-sample interval. C, Coherence z-score difference (Unpredictable minus Predictable) between each area and the rest, separately for superficial coherence to rest (orange bars) and deep coherence (blue bars) to rest (blue bars) for different frequency ranges (gamma: upper

subpanel, beta: second from the top sub-panel, alpha: second from the bottom sub-panel, theta: bottom subpanel). Mean +/- SEM, asterisks denote significant differences between layers.

Supplemental Figure 12 | Unpredicted vs. Predicted Granger causality in the sample interval

Z-score of Granger causality (GC) differences: Unpredicted minus Predicted, divided by the standard error of the mean for each area combination. Red bars denote Unpredicted > Predicted GC, blue bars Unpredicted < Predicted GC, $p<0.05$, cluster-based randomization test. Mean +/- SEM across all bipolar LFP pairs for each inter-areal combination. The upper right interactions are feedforward, the lower left interactions are feedback.

Supplemental Figure 13 | Coupling matrix between higher-order cortex LFP power and MUA and gamma in V4

Regression coefficients between trial-by-trial MUA/gamma power in superficial/deep layers of V4 (y axis) and LFP power in higher-order cortical areas LIP, 7A, FEF, and PFC. Areas PFC and 7A had laminar resolution, LIP and FEF did not. Regression coefficients were extracted for each session separately, and the median value across all available sessions is depicted (V4xLIP interaction, N = 36 sessions; V4x7A interaction, N = 30 sessions; V4xFEF interaction, N = 43 sessions; V4xPFC interaction, N = 45 sessions). Significantly non-zero coefficients (sign test of regression weights across sessions, $P<0.05$) are indicated with opaque colors. A, Regression coefficients for theta (2-6 Hz), B, Regression coefficients for alpha (8-14 Hz), C, Regression coefficients for beta (15-30 Hz), D, Regression coefficients for gamma (40-90 Hz).

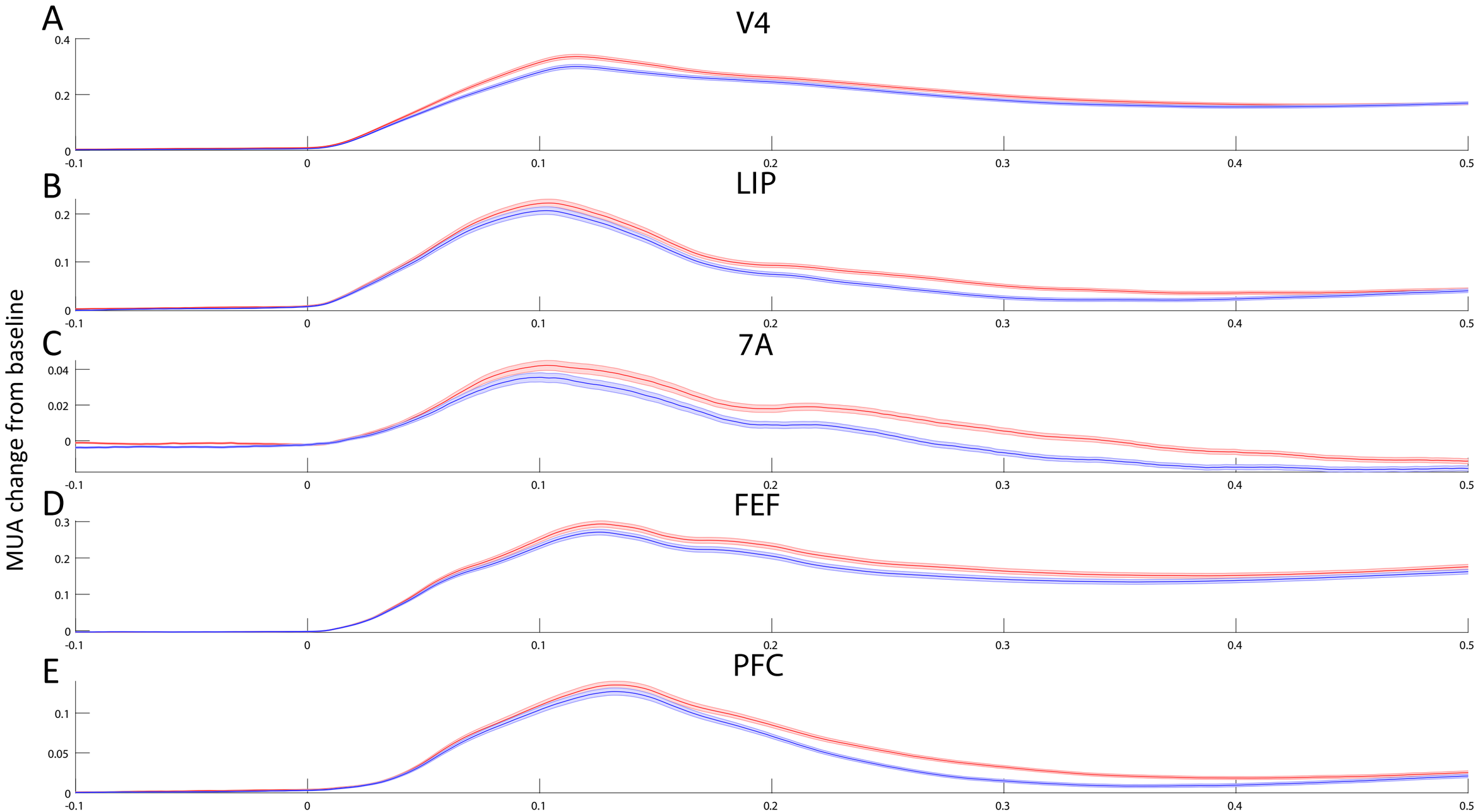

Supplemental Figure 1

A

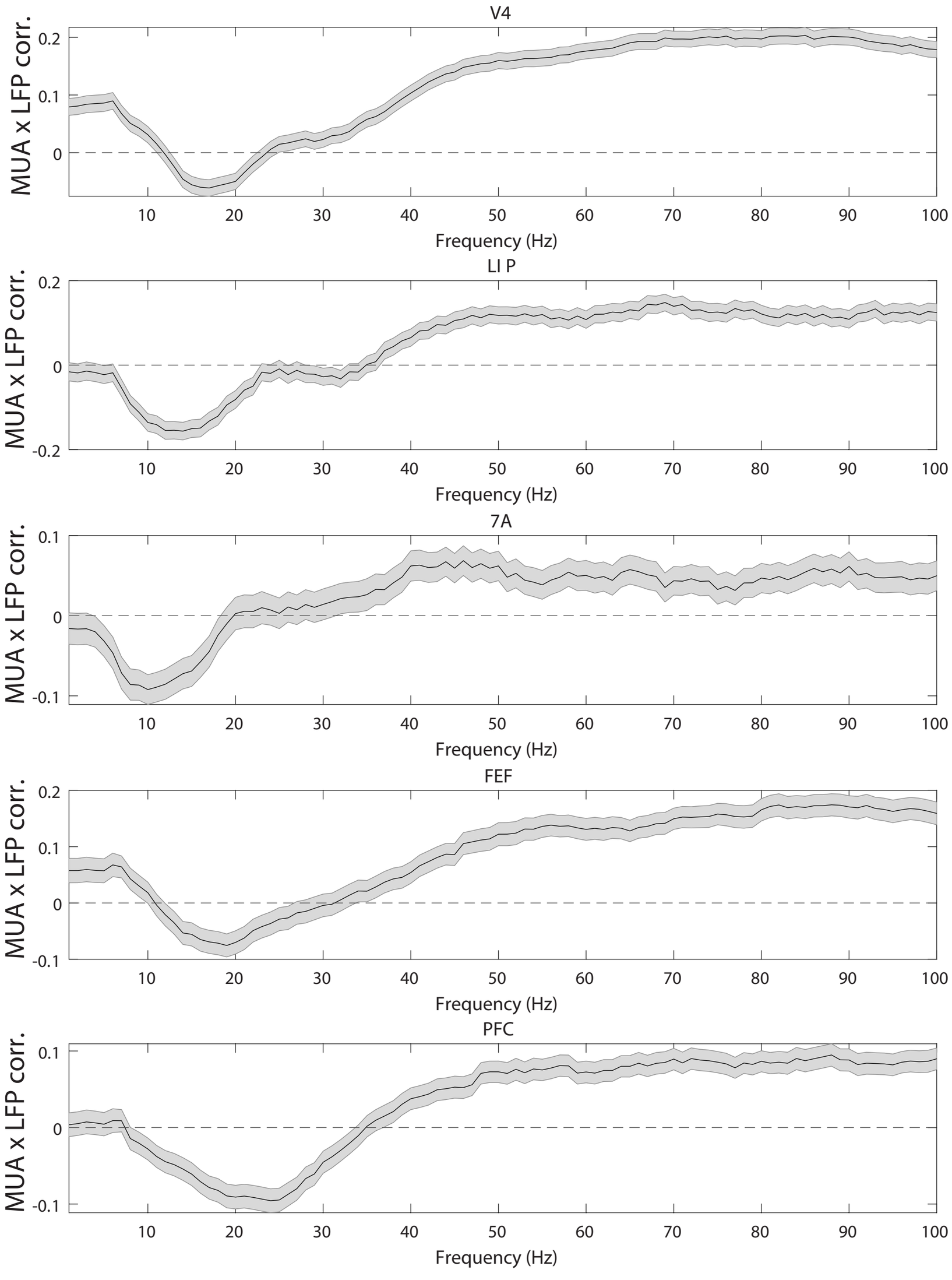

B

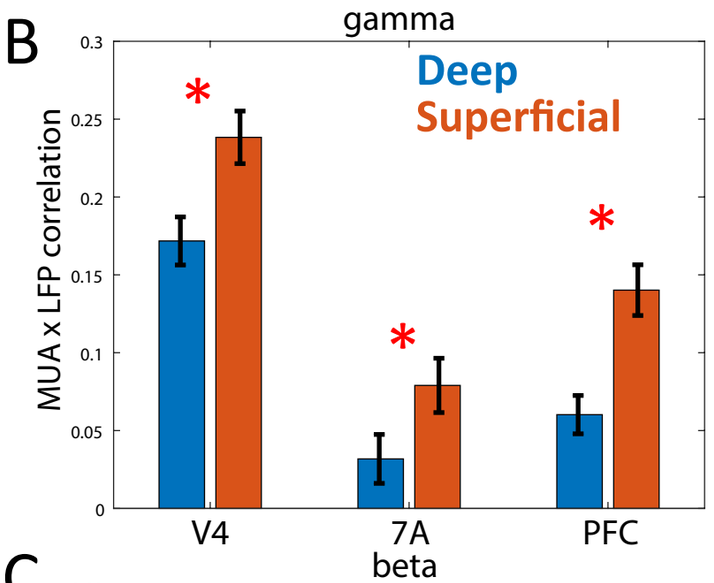

C

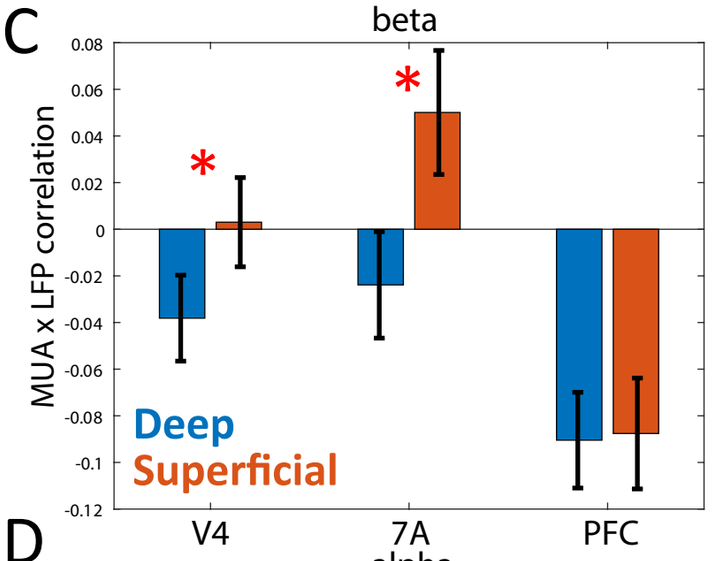

D

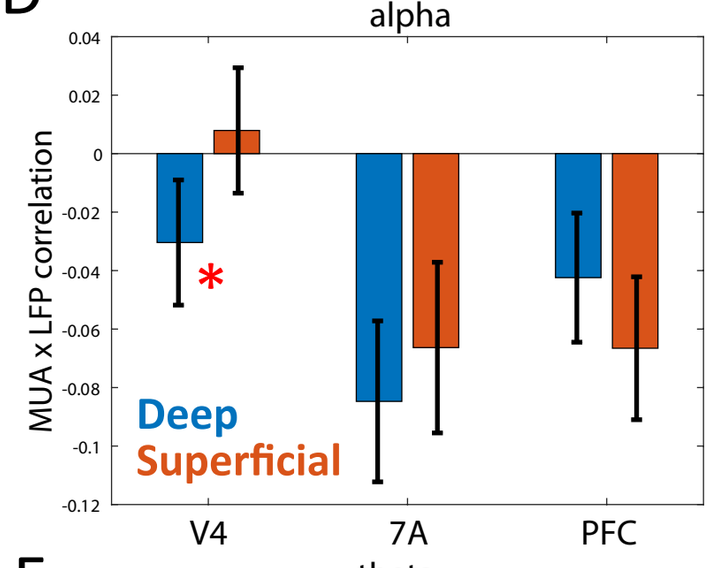

E

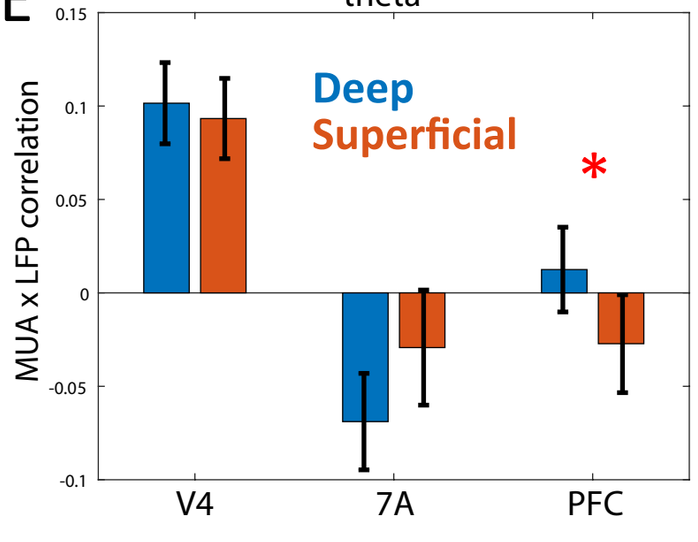

Supplemental Figure 2

A

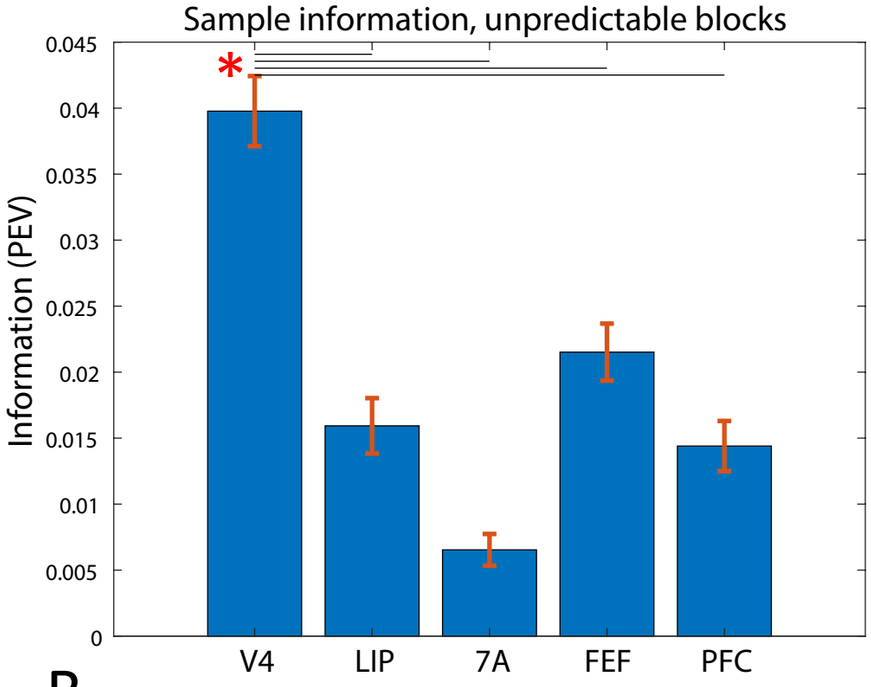

B

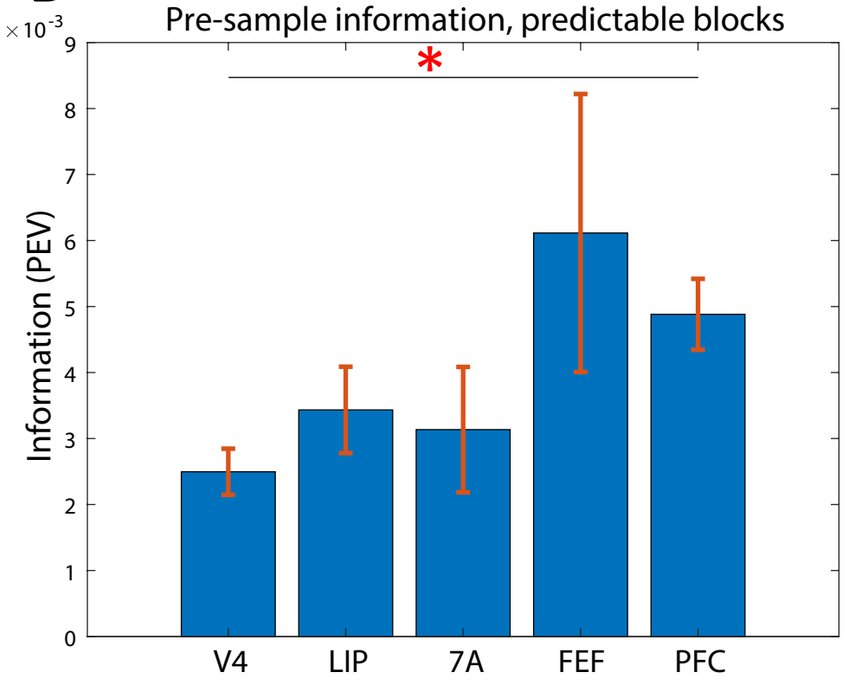

C

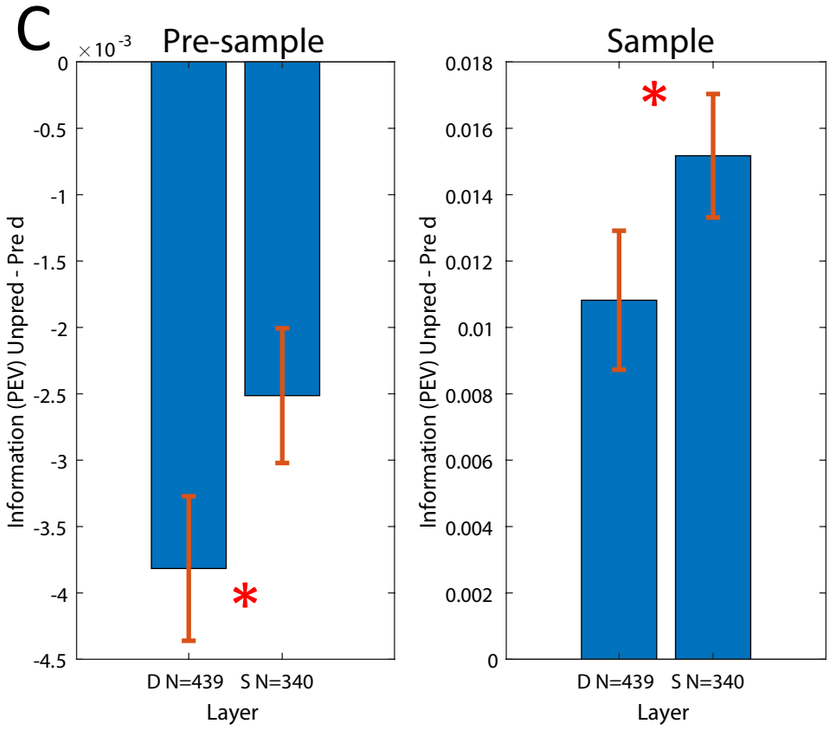

D

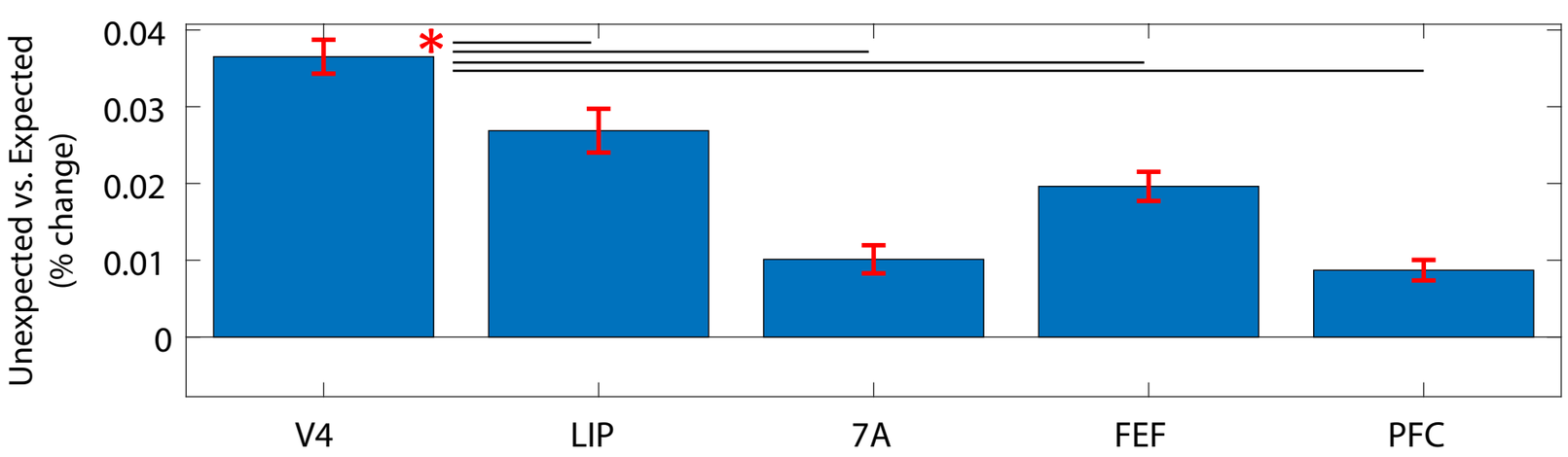

E

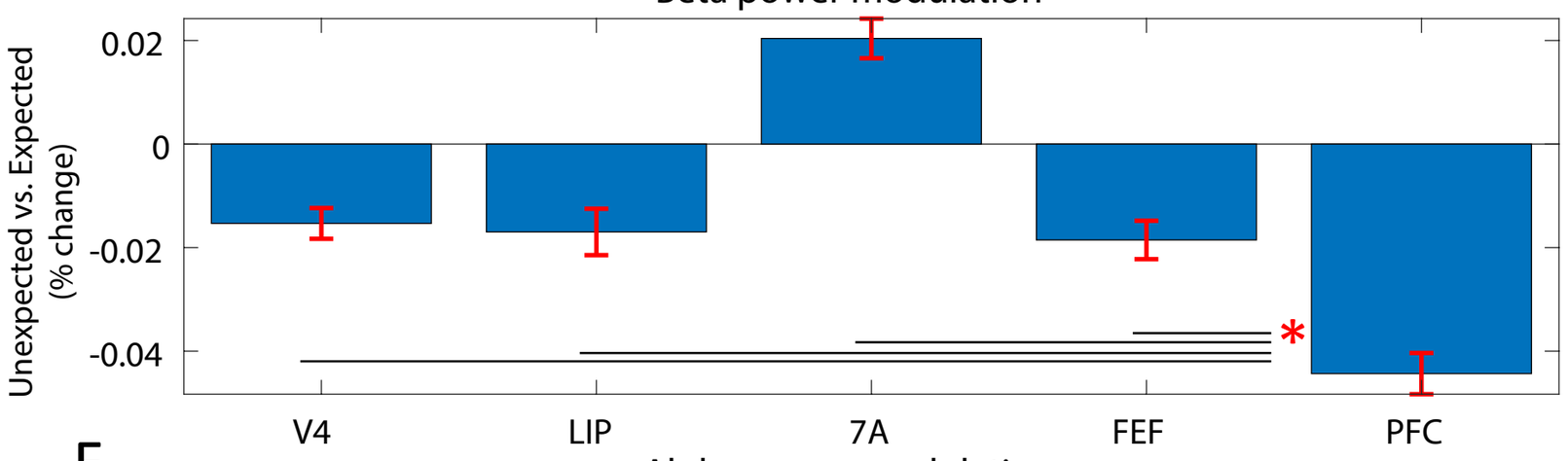

F

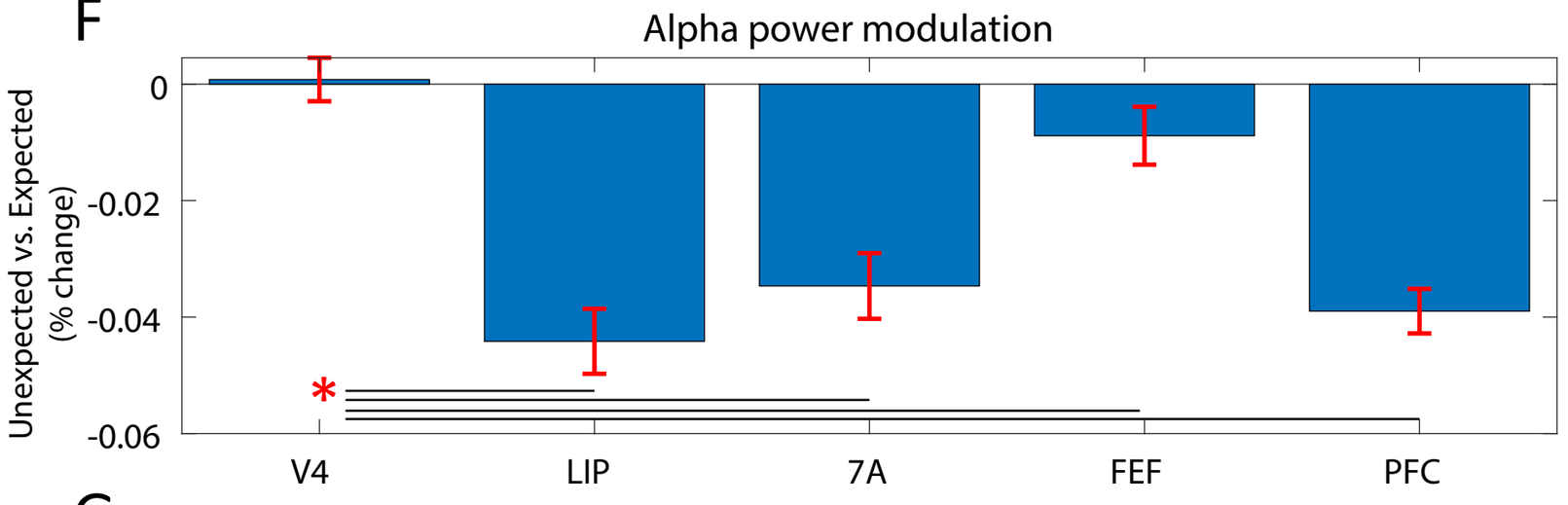

G

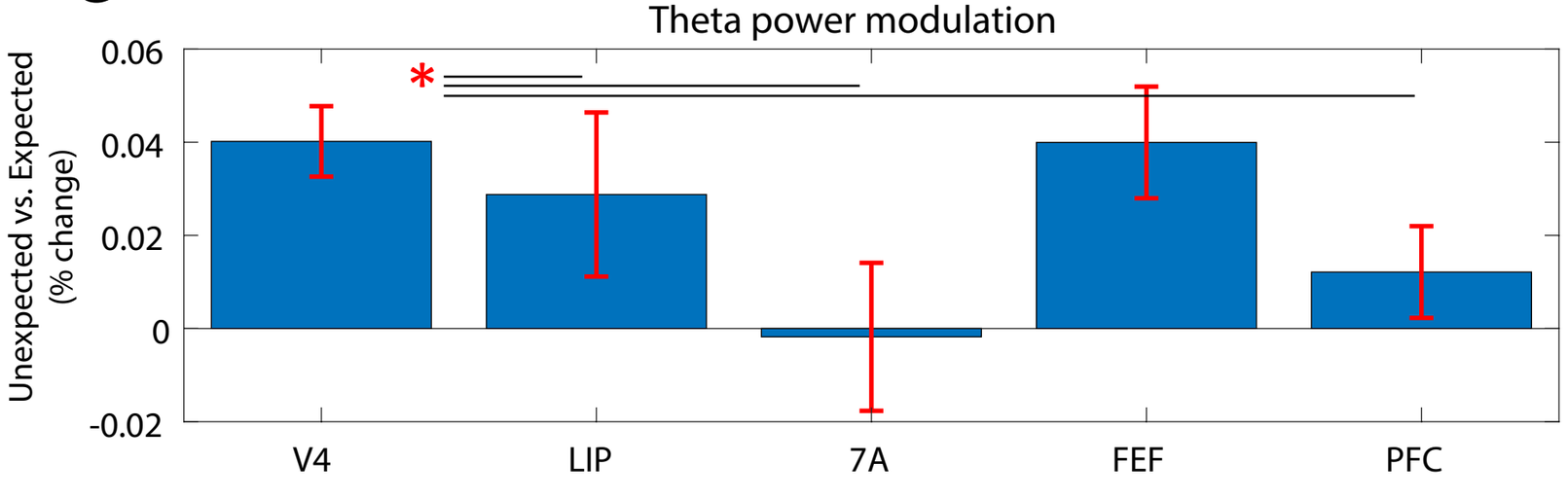

Supplemental Figure 3

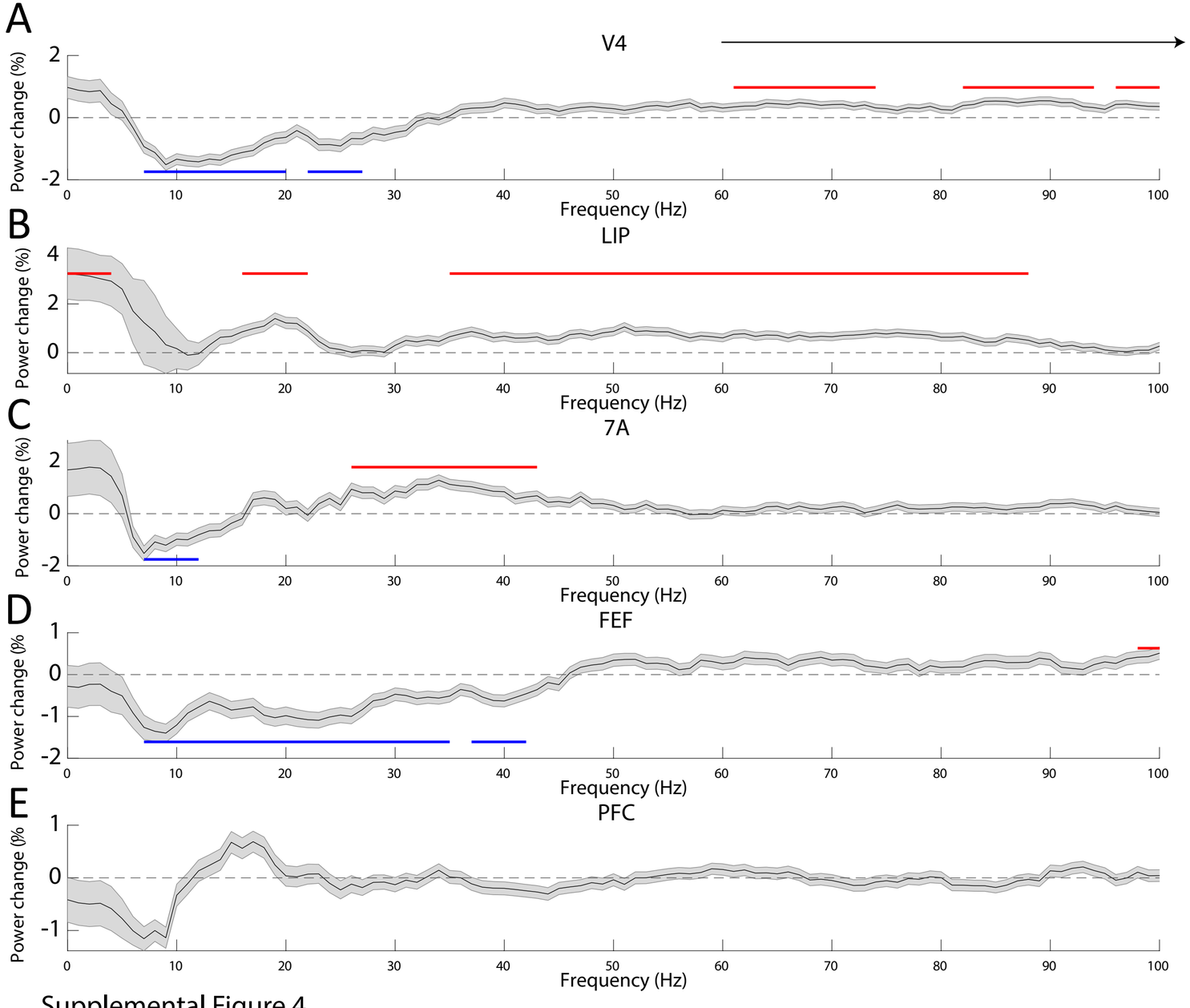

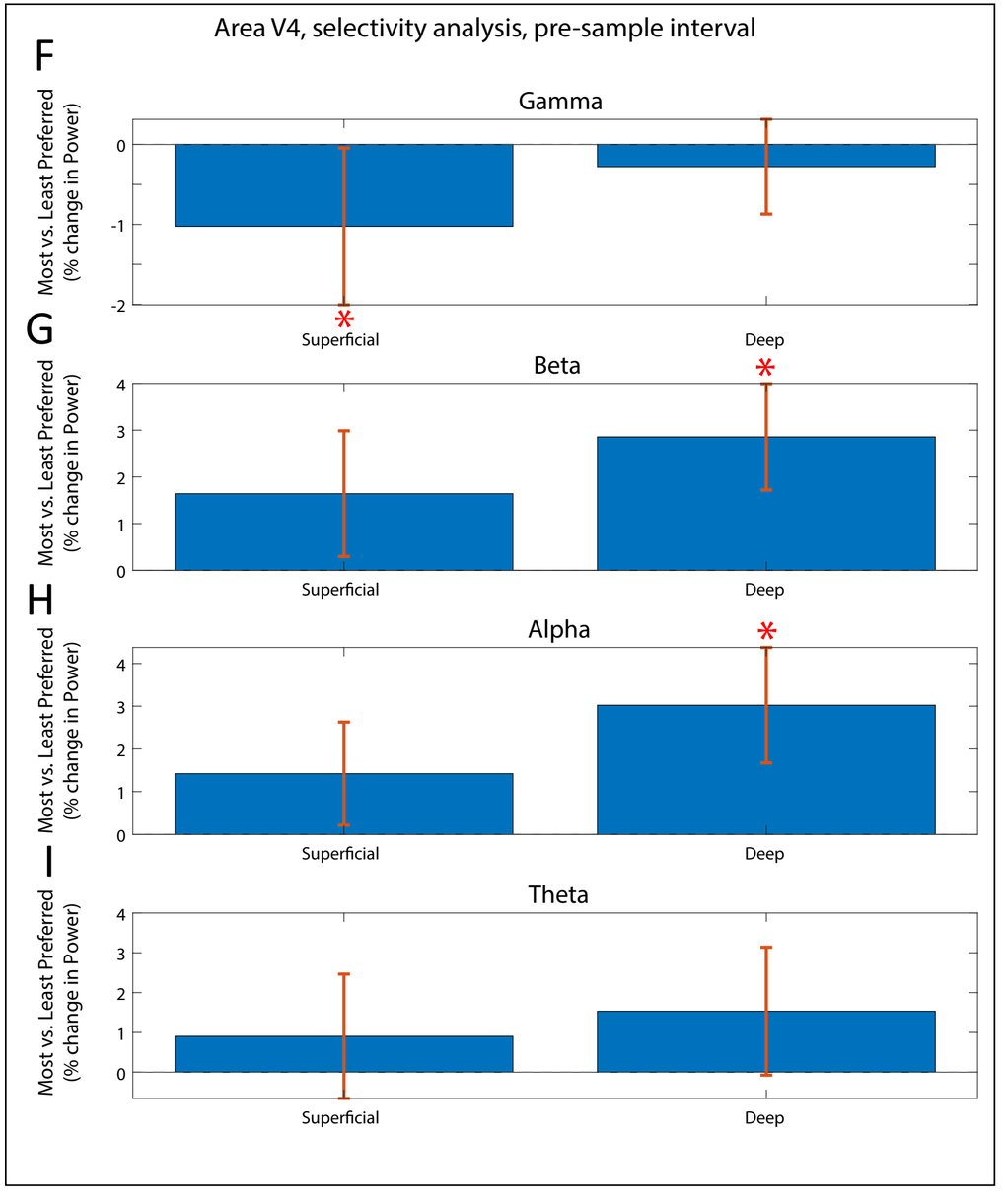

Supplemental Figure 4

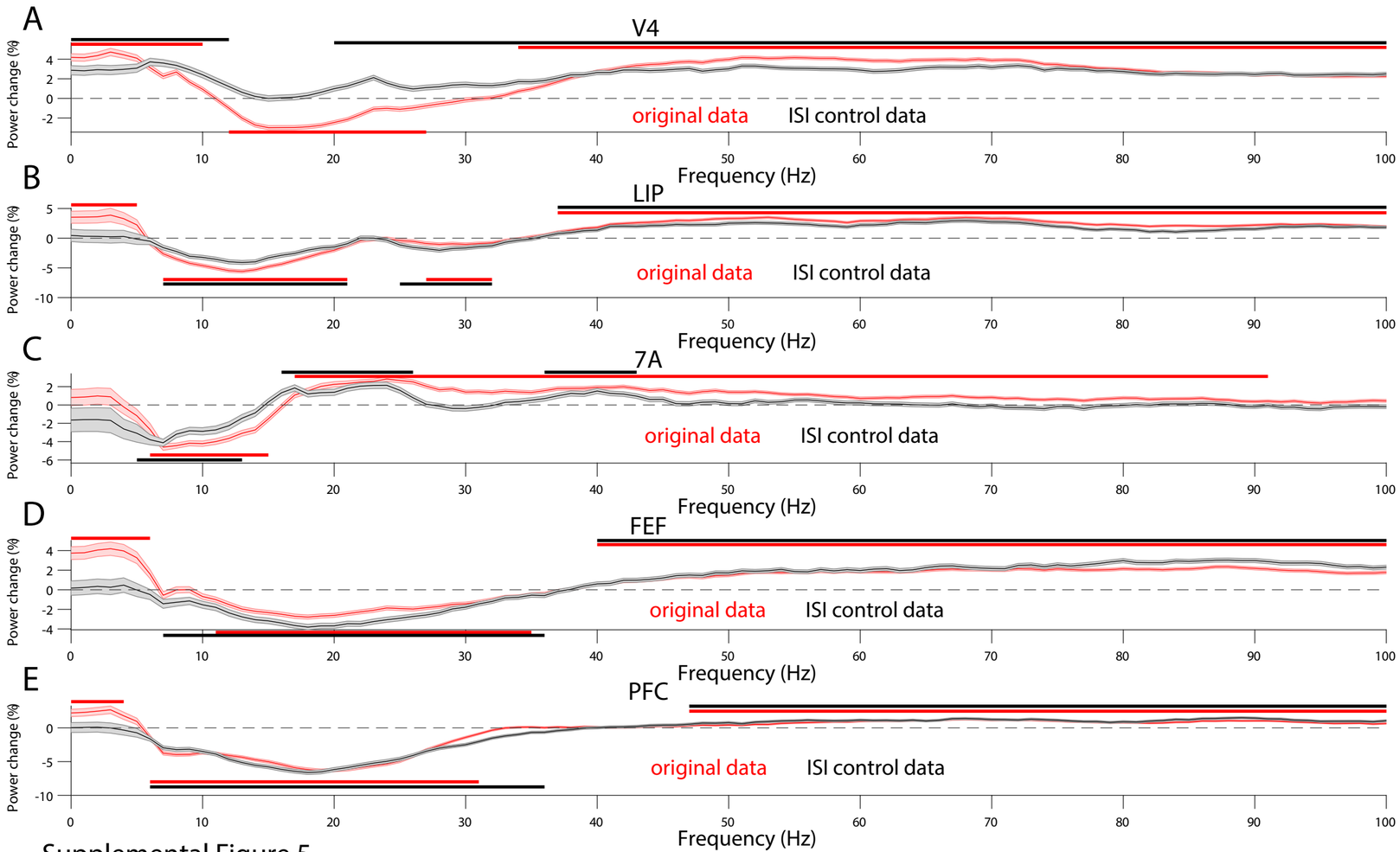

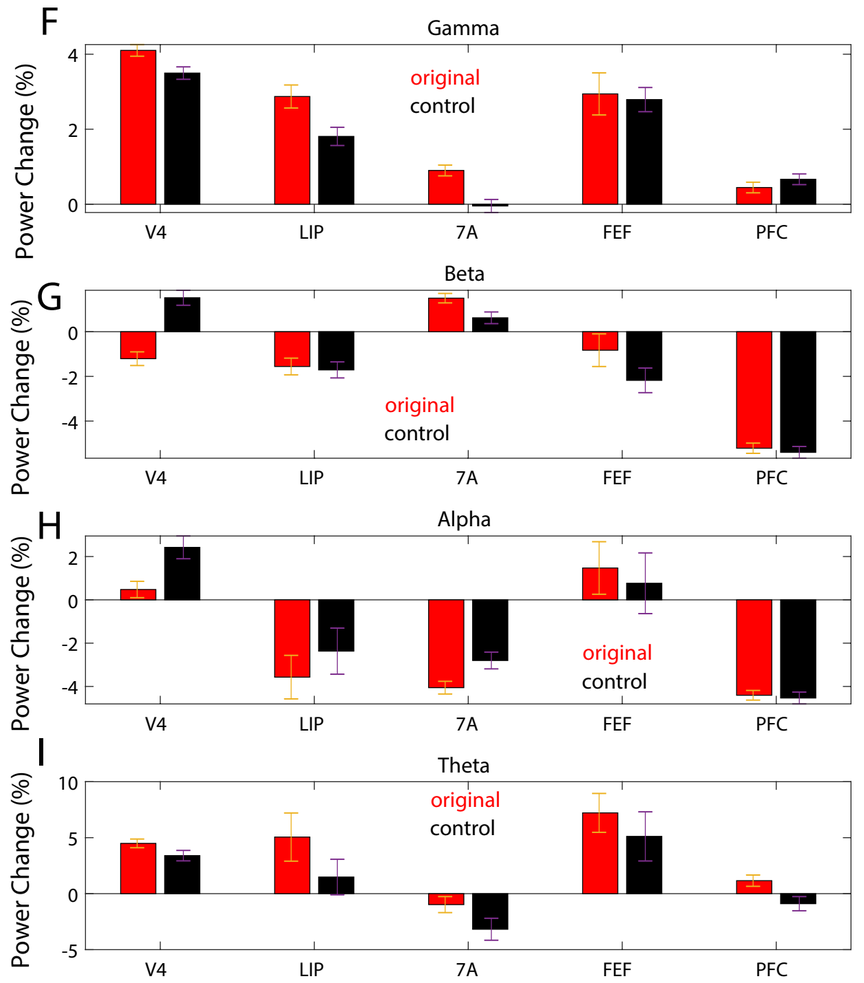

Supplemental Figure 5

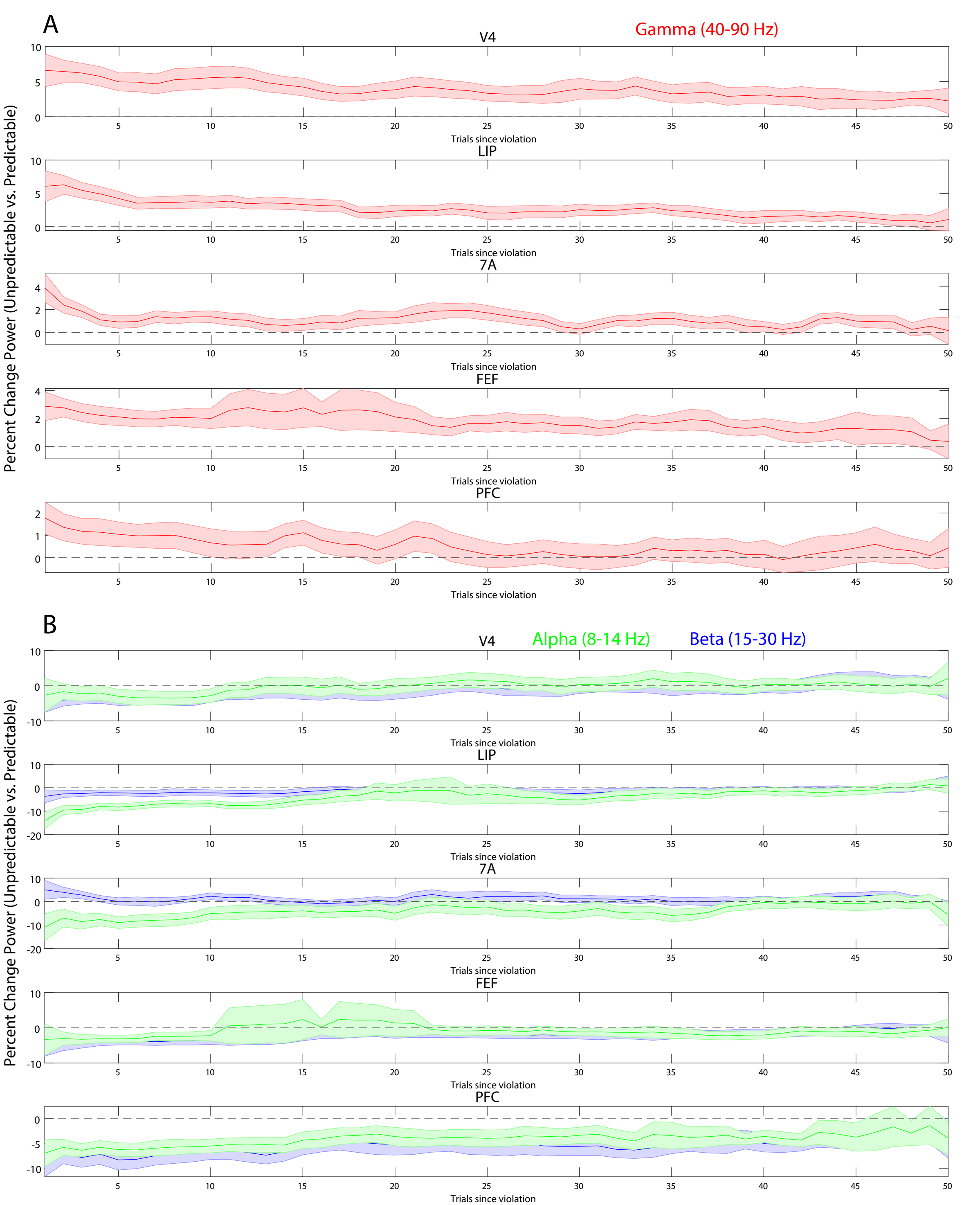

Supplemental Figure 6

A

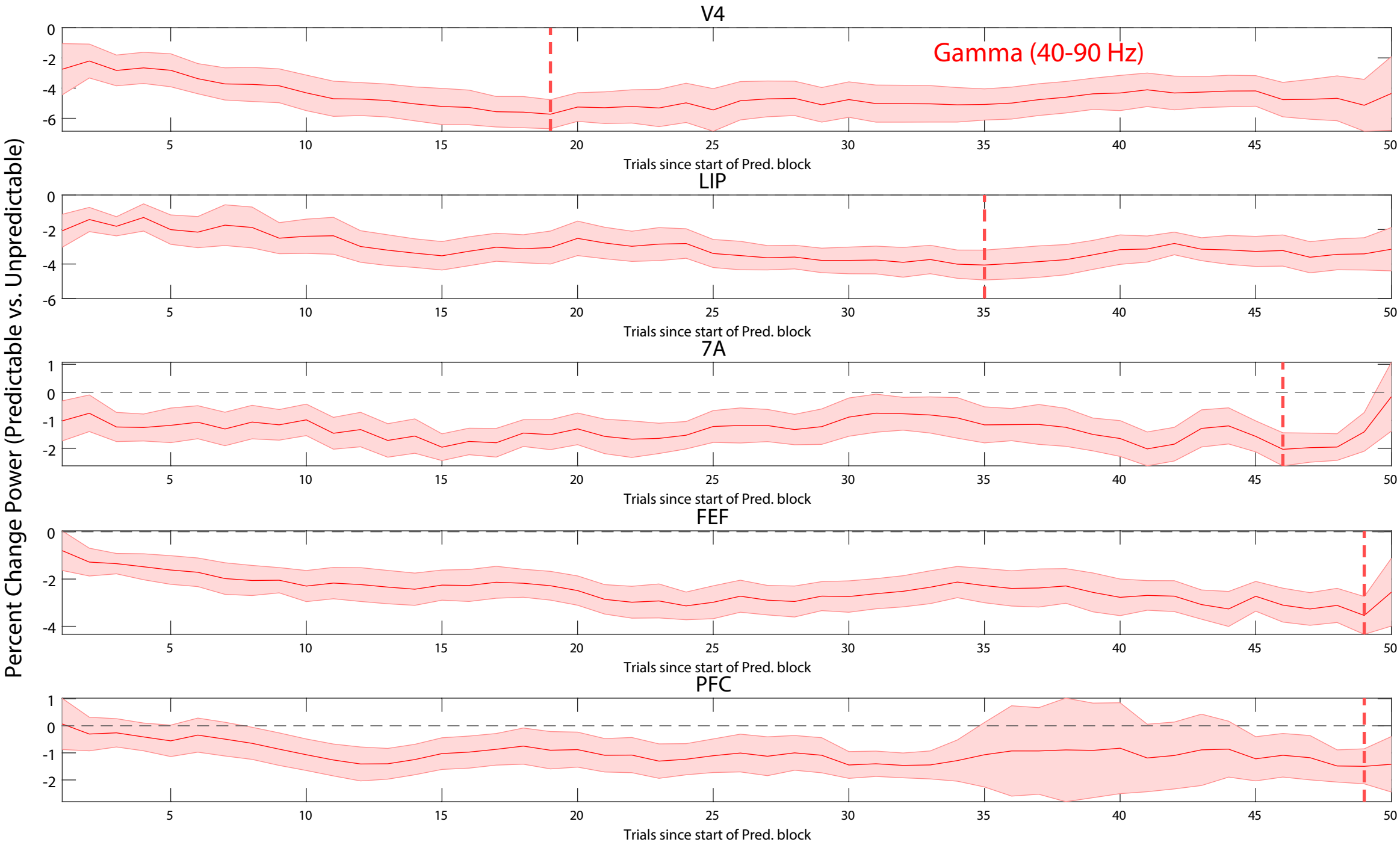

B

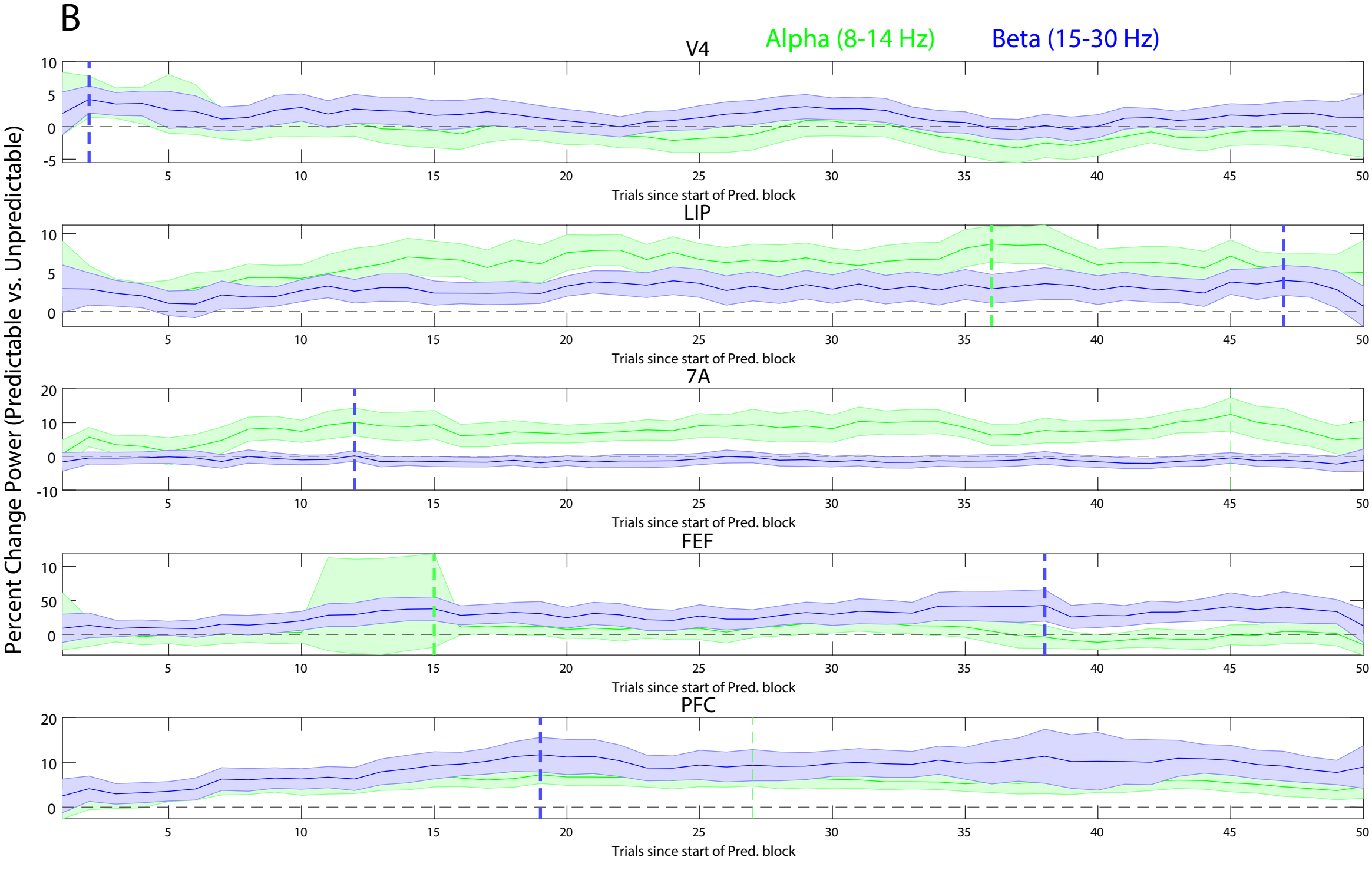

Supplemental Figure 7

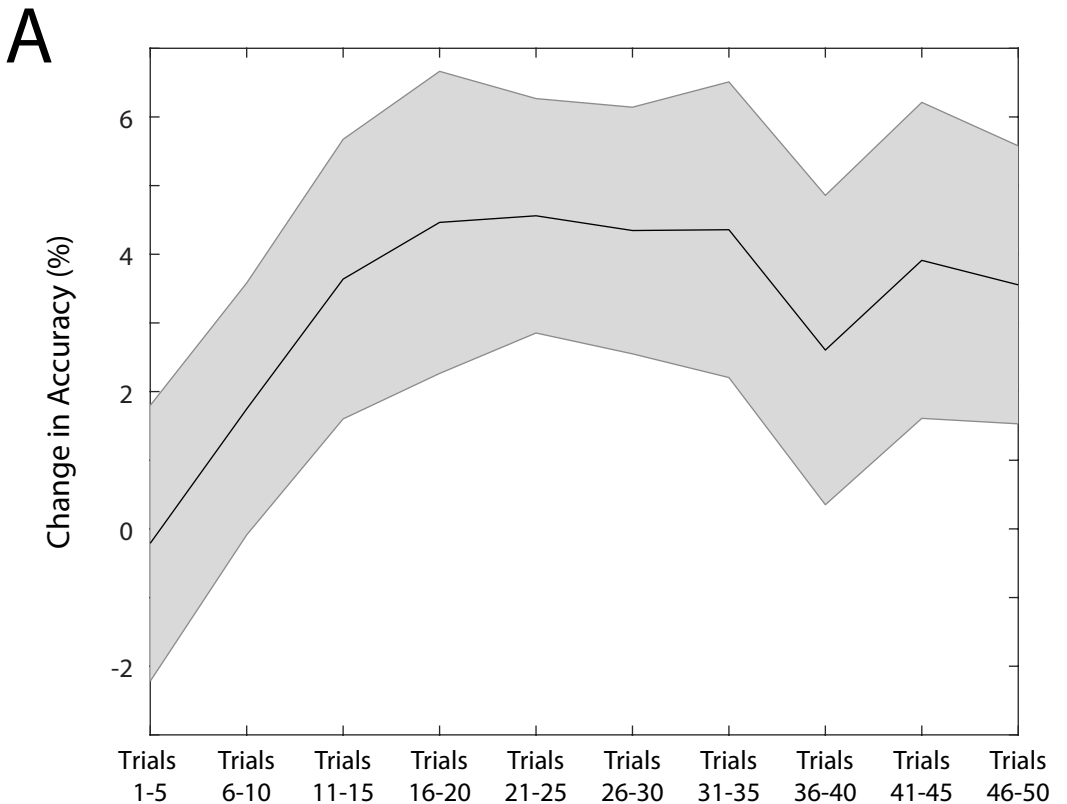

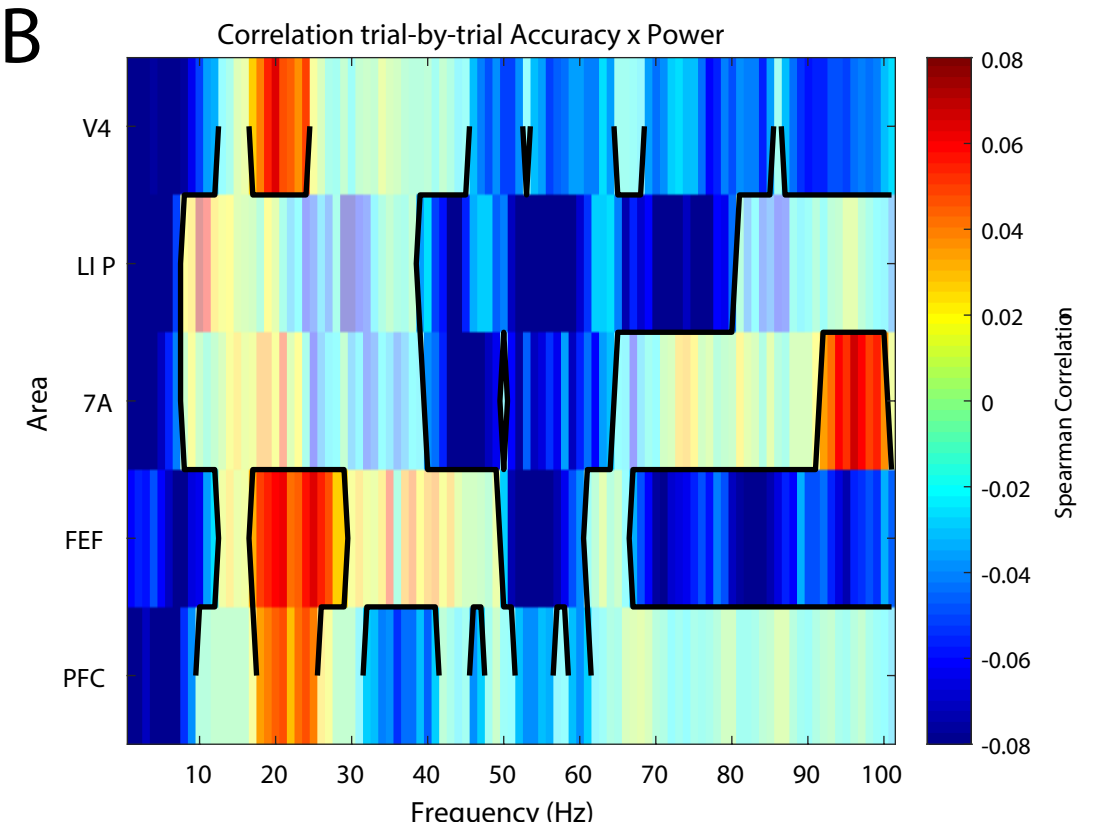

Supplemental Figure 8

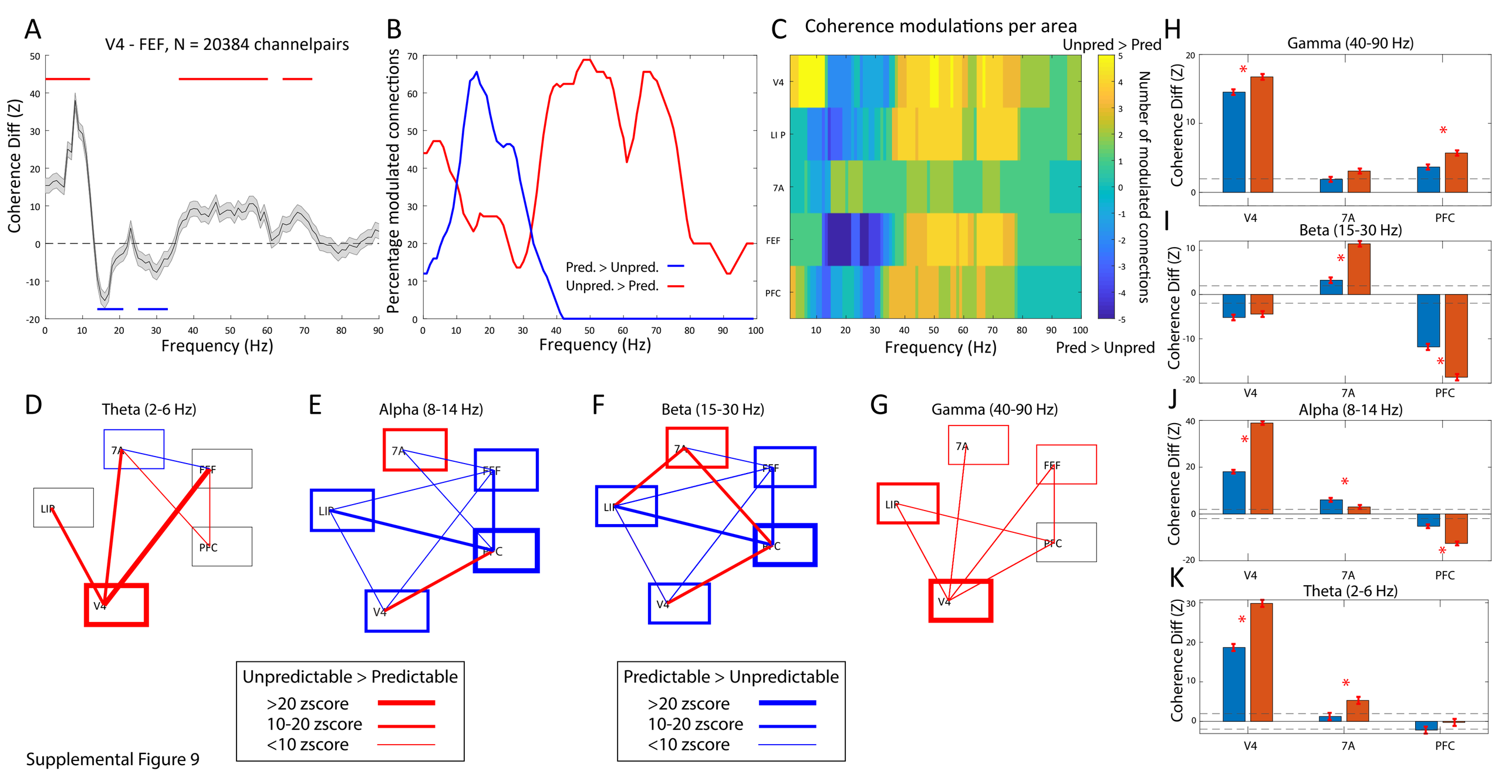

Supplemental Figure 9

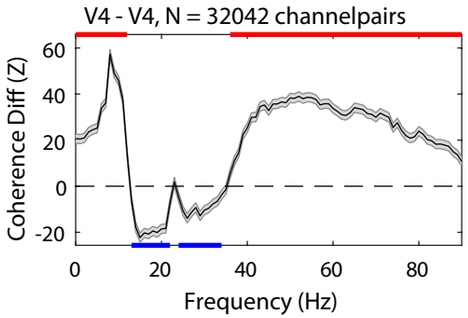

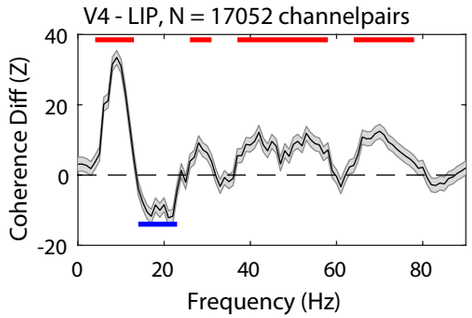

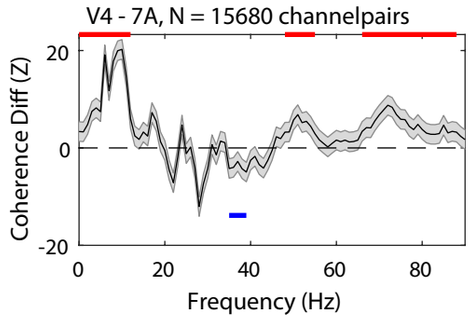

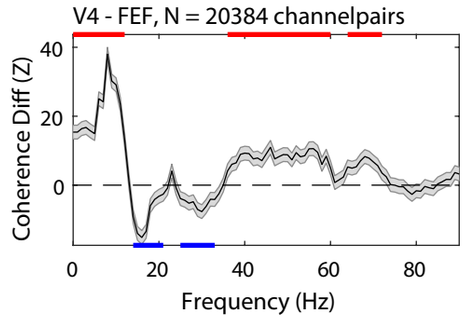

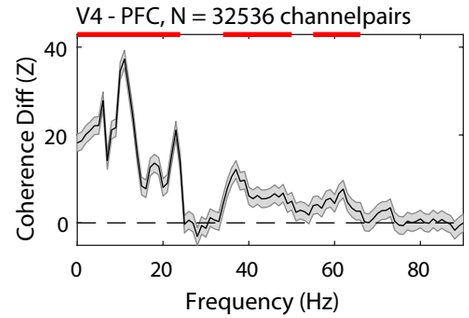

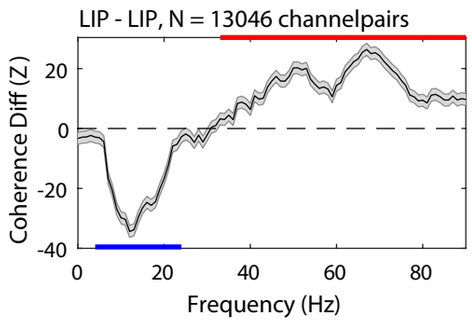

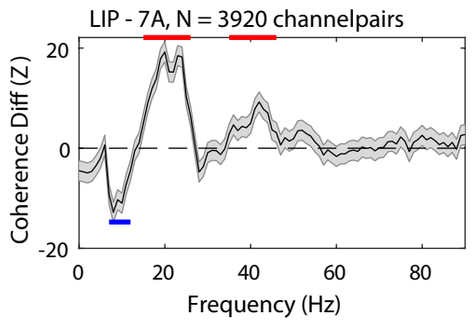

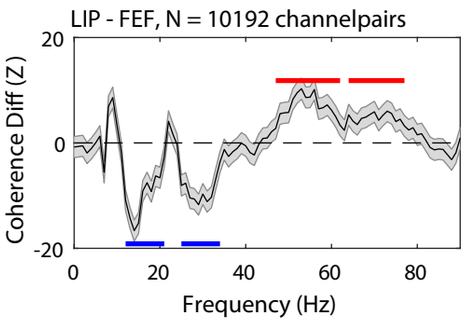

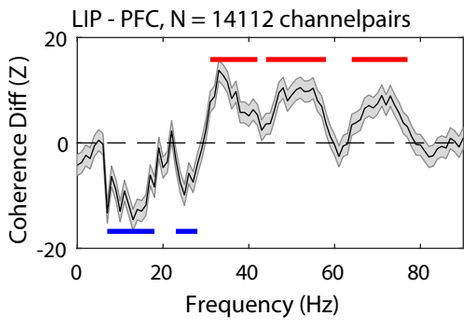

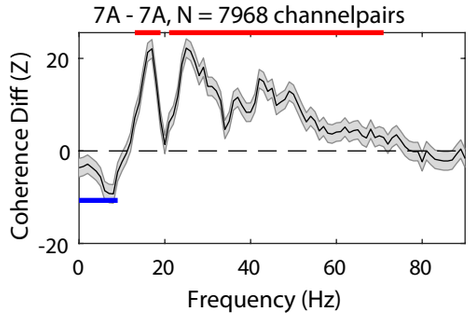

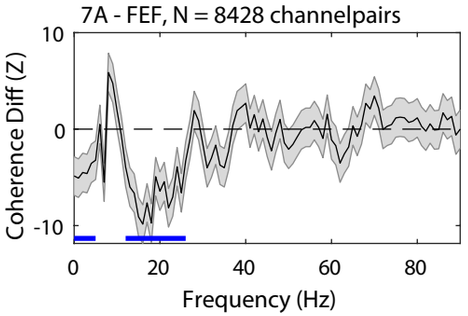

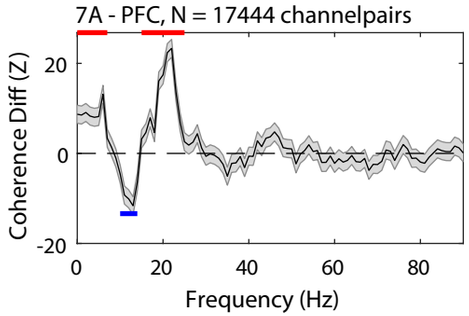

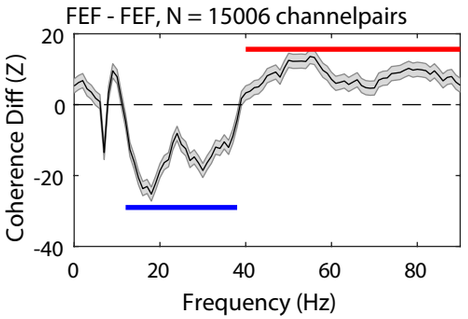

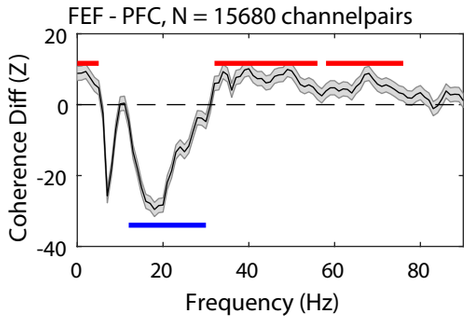

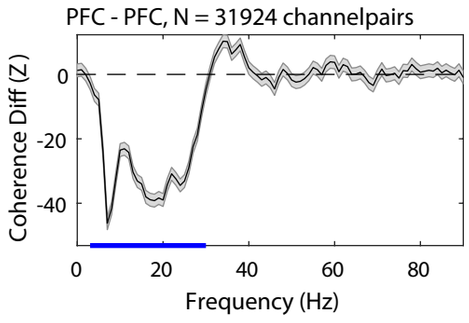

p<0.05, corrected for multiple comparisons

p<0.05, corrected for multiple comparisons

Supplemental Figure 10

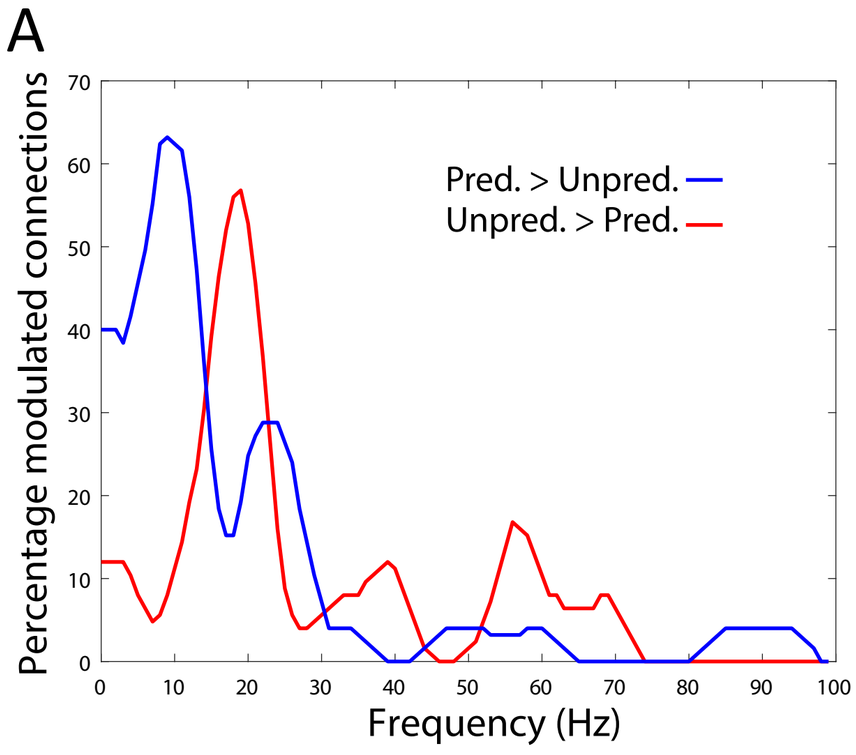

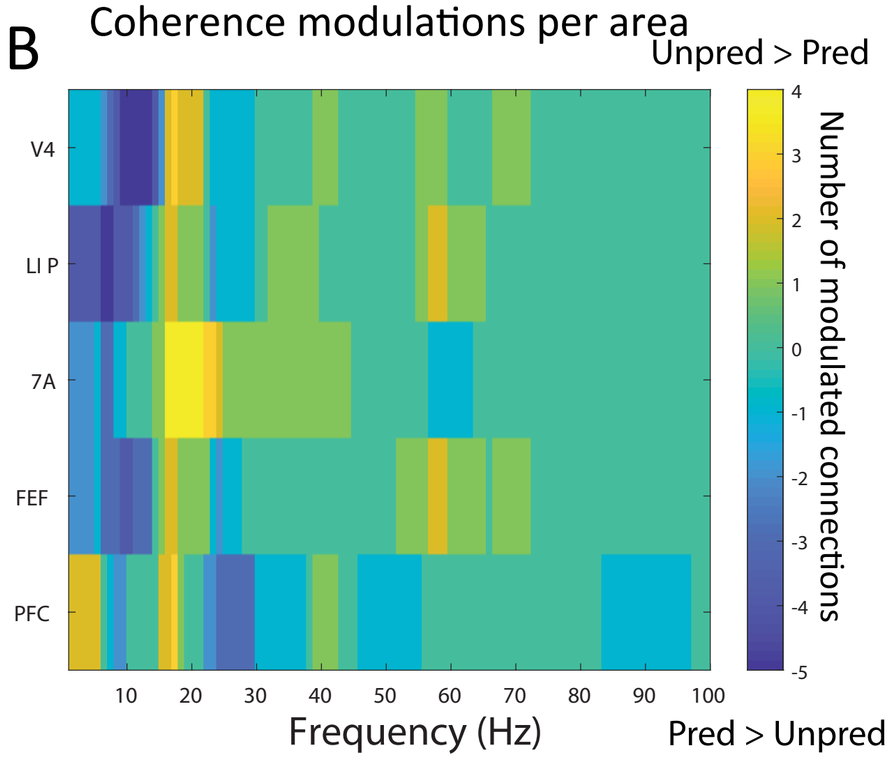

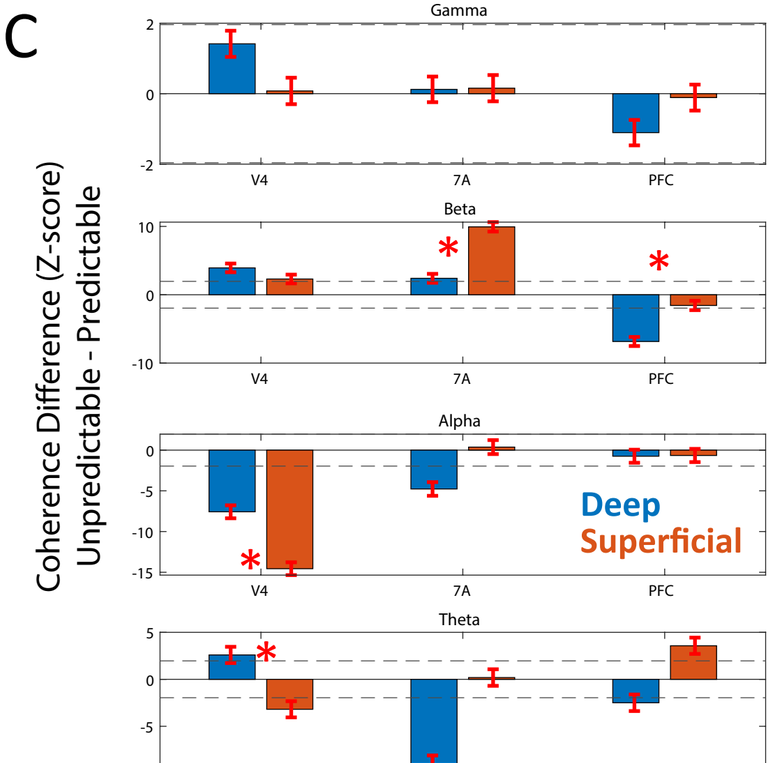

Supplemental Figure 11

Supplemental Figure 12

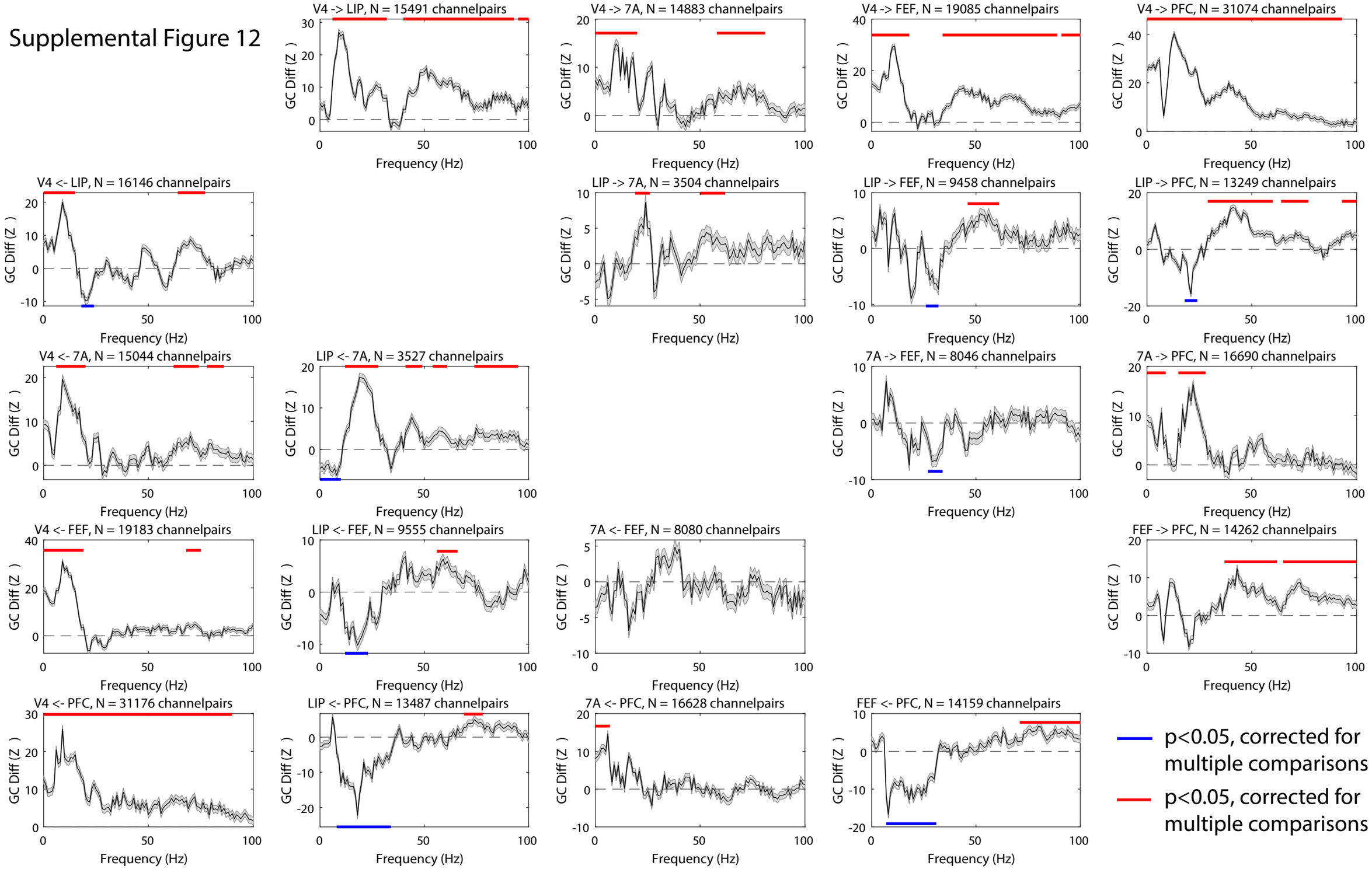

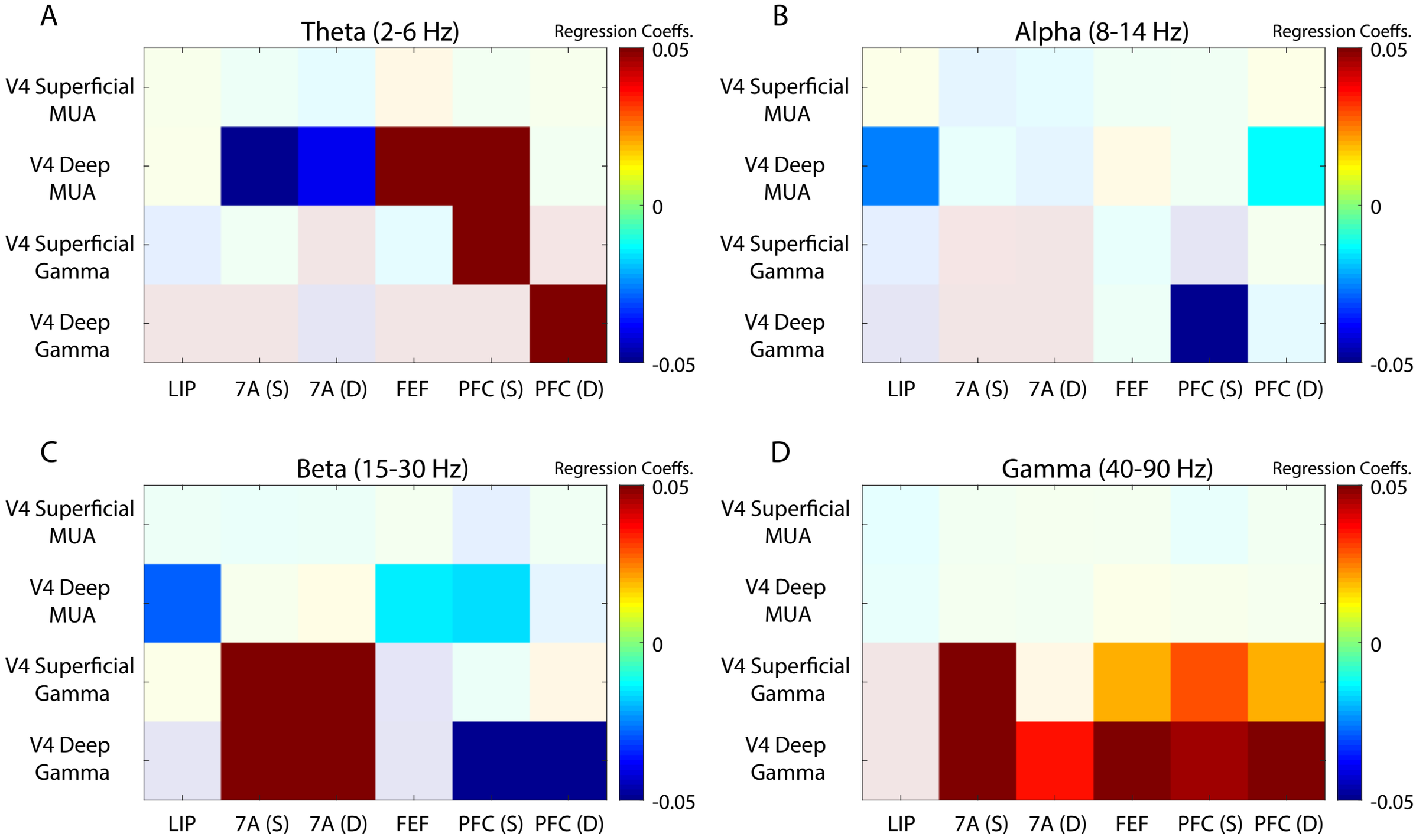

Supplemental Figure 13